

ABSTRACT

Title of Thesis: SPHERICAL GAS-FUELED COOL
DIFFUSION FLAMES

Minhyeng Kim, Master of Science, 2022

Thesis Directed By: Professor Peter B. Sunderland, Department of
Fire Protection Engineering

An improved understanding of cool diffusion flames could lead to improved engines. These flames are investigated here using a spherical porous burner with gaseous fuels in the microgravity environment of the International Space Station. Normal and inverse flames burning ethane, propane, and *n*-butane were explored with various fuel and oxygen concentrations, pressures, and flow rates. The diagnostics included an intensified video camera, radiometers, thin-filament pyrometry, and thermocouples. Spherical cool diffusion flames, transitioned from hot flames, burning gases were observed for the first time. However, these cool flames were not readily produced and were only obtained for normal *n*-butane flames at 2 bar with an ambient oxygen mole fraction of 0.39. The sizes of hot and cool diffusion flames were investigated with the intensified camera images. The hot flames that spawned the cool flames were 2.6 times as large. An analytical model is presented that combines previous models for steady droplet burning and the partial-burning regime for cool diffusion flames. The results identify the importance of burner temperature on the behavior of these cool flames. They also indicate that the observed cool flames reside in rich regions near a mixture fraction of 0.53.

SPHERICAL GAS-FUELED COOL DIFFUSION FLAMES

by

Minhyeng Kim

Thesis submitted to the Faculty of the Graduate School of the
University of Maryland, College Park, in partial fulfillment
of the requirements for the degree of
Master of Science
2022

Advisory Committee:

Professor Peter B. Sunderland, Chair

Professor Arnaud Trouvé

Professor Stanislav I. Stoliarov

© Copyright by
Minhyeng Kim
2022

Acknowledgments

First and foremost, I would like to express my gratitude to my advisor Prof. Sunderland for the continuous support of my study, his enthusiasm, and great academic insights. His guidance and encouragement helped me in my research and writing of this thesis. I could not have imagined finishing my thesis without his support.

I also would like to thank the thesis committee member, Prof. Trouvé and Prof. Stoliarov, for their great interest in my study, encouragement, and insightful comments.

I would also like to wish my deepest thanks to the coauthors of the conference papers, Mr. Waddella, Dr. Nayagam, Mr. Stocker, Mr. Dietrich, Dr. Ju, Dr. Williams, Dr. Irace, and Dr. Axelbaum, for their guidance and knowledge. The papers could not have been completed without their support.

I would like to thank the ISS crew members and the ISS operations team for their support and cooperation. Their timely workmanship and hard work allowed the project to be completed successfully.

Last but not least, I would like to thank my family. Thanks to my parents for their love and support, which meant a lot to me. My deepest gratitude to my loving wife, Woohey, and my daughter, Haryn. It must have been difficult for them to move to another country, but they have been through the hard times with me and gave me so much love and support.

Table of Contents

Acknowledgements	ii
Table of Contents	iii
List of Tables	iv
List of Figures	iv
Chapter 1 : Introduction	1
1.1 Background	1
1.2 Motivation and Objective	6
Chapter 2 : Experiments	8
2.1 Experimental Setup	8
2.2 Diagnostics	10
2.3 Operation of Experiments	13
Chapter 3 : Analytical	15
3.1 Normal Flames	15
3.2 Inverse Flames	19
Chapter 4 : Results and Discussion	22
4.1 Cool Flame Observation	22
4.2 Images of Cool Flames	24
4.3 Radiometer Readings on Cool Flames	26
4.4 Hot and Cool Flame Size	29
4.5 Conditions for Cool Flames	33
Chapter 5: Conclusions	34
Appendix A. MATLAB Code for the Flame Size Estimation	35
Appendix B. Plots of Measurements with Tim	36
Appendix C. Hot Flame Images and Their Size by Fitting the Contour of Peak Intensity with a Circle	39
Appendix D. Cool Flame Images and Distance between Two Peaks	42
Appendix E. CFI-G Test Matrices	46
Appendix F. CFI-G Test Parameters	55
Bibliography	57

List of Tables

Table 4.1 Summary of the hot and cool flames observed.....	22
Table 4.2. Summary of the cool flames observed ^a	23
Table E.1. Corresponding test point numbers to the test IDs in Table 4.2	46
Table E.2. CFI-G test matrix for test day 21088, 21102, and 21106 (normal flames).....	47
Table E.3. CFI-G test matrix for test day 21112 and 21125 (normal flames)	48
Table E.4. CFI-G test matrix for test day 21130, 21137, and 21153 (normal flames).....	49
Table E.5. CFI-G test matrix for test day 21162, 21174, and 21291 (normal flames).....	50
Table E.6. CFI-G test matrix for test day 21196, 21202, and 21209 (inverse flames).....	51
Table E.7. CFI-G test matrix for test day 21216, 21222, 21228, and 21235 (inverse flames).....	52
Table E.8. CFI-G test matrix for test day 21242, 21256, 21265, and 21270 (inverse flames).....	53
Table E.9. CFI-G test matrix for test day 21277 (inverse flames).....	54
Table F.1. CFI-G test parameters for cool flame conditions (part 1)	55
Table F.2. CFI-G test parameters for cool flame conditions (part 2)	56

List of Figures

Fig. 1.1. Dibutyl-ether (DBE) mole fraction profile in jet-stirred reactor under fuel-rich conditions ($\phi = 2$), at 10 atm and for $\tau = 700$ ms [9].	2
Fig. 1.2. Computed low temperature ignition and high temperature ignition of <i>n</i> -heptane/air mixtures by a kinetic model. Ignition temperature as a function of time at 20 atm and equivalent ratio of 0.4 at 700 K and 1000 K, respectively [2].	3
Fig. 1.3. Examples of radiative extinction and subsequent second-stage combustion of <i>n</i> -heptane droplets [7].	4
Fig. 1.4. Direct photos of cool (a) and hot (b) diffusion flames, observed at the identical flow condition, fuel mole fraction (X_f) = 0.07 and strain rate (a) = 100 s^{-1} [5].	5
Fig. 2.1. Solid model representation of the ACME chamber insert [32].	8
Fig. 2.2. The spherical porous burner and its assembly prior to testing [32].	9
Fig. 2.3. Fibers used for TFP analysis: (a) hot flame image by the digital camera, (b) glowing fibers in a hot flame with the same conditions of (a), and (c) fiber array [32].	11
Fig. 2.4. Solid model representation of radiometer layout [32].	12
Fig. 2.5. Schematic layout of the ACME insert diagnostics (cross sectional view): (a) analog camera, (b) digital camera, (c) intensified camera, (d) radiometer array, and (e) PMTs [32].	13
Fig. 3.1. Temperature T versus mixture fraction in the partial-burning regime for a normal cool diffusion flame, reproduced from Nayagam et al. [34].	17
Fig. 3.2. Model predictions of normal cool diffusion flames for the conditions of $\dot{m}_{HC} = 1.5 \text{ mg/s}$, $r_s = 3.2 \text{ mm}$, $T_\infty = 300 \text{ K}$, $Z_{st} = 0.20$, and $\rho D = 0.0334 \text{ g/m-s}$ at 300 K. .	18

Fig. 3.3. Temperature T versus mixture fraction in the partial-burning regime for an inverse cool diffusion flame.....	20
Fig. 3.4. Model predictions of inverse cool diffusion flames in the ambient filled with n -butane. The conditions are as follows: $\dot{m}_{O_2} = 5.37$ mg/s, $r_s = 3.2$ mm, $T_\infty = 300$ K, $Z_{st} = 0.44$, and $\rho D = 0.0334$ g/m-s at 300 K.	21
Fig. 4.1. Sequential intensified camera images of Test D, from the ignition to the extinction.....	24
Fig. 4.2. Intensified camera images from Test D of (a) the hot flame and (b) the cool flame. The false colors here were obtained by matching the colors of microgravity hot flames and normal gravity cool flames. The times after ignition, t , are shown. The dashed circles indicate the burner location. Image (b) is an average of images from the times shown and has an exposure 50 times as bright as that of (a).	25
Fig. 4.3. Sequential intensified camera images of Test F. The flame was ignited ($t = 0$ s) and transitioned to a cool flame after oscillations ($t = 92.5$ s). The glow due to the type B thermocouple was growing as time increased, and reignited a hot flame ($t = 97.2$ s).....	26
Fig. 4.4. Temporal plots of measurements for (a) a hot flame at $\dot{m}_{HC} = 2$ mg/s that extinguishes and (b) a hot flame at $\dot{m}_{HC} = 1.5$ mg/s that transitions to a cool diffusion flame (Test D).	27
Fig. 4.5. Temporal plots of measurements for multiple hot-cool flame transitions at $\dot{m}_{HC} = 1.5$ mg/s (Tests G1-G5).	28
Fig. 4.6. The contour of peak intensity with a circle and its radius in pixels for Test A found by using a MATLAB algorithm.	30

Fig. 4.7. Averaged image of the cool flame of Test G1 and a plot of the pixel values along the dashed line. The white streak in front of the burner tube is the type B thermocouple's double reflection off the camera lens and the window.	31
Fig. 4.8. Measured versus modeled flame radii for hot and cool flames. The droplet cool flame is from [34]. The data has a coefficient of determination of $R^2 = 0.92$ with respect to the line shown with unity slope.	32
Fig. A.1. MATLAB code for the flame size estimation	35
Fig. B.1 Temporal plots of measurements for a hot flame at $\dot{m}_{HC} = 1.0$ mg/s that transitions to a cool diffusion flame (Test B).	36
Fig. B.2. Temporal plots of measurements for a hot flame at $\dot{m}_{HC} = 0.75$ mg/s that transitions to a cool diffusion flame (Test A).	36
Fig. B.3. Temporal plots of measurements for a hot flame at $\dot{m}_{HC} = 1.0$ mg/s that transitions to a cool diffusion flame (Test E).....	37
Fig. B.4. Temporal plots of measurements for a hot flame at $\dot{m}_{HC} = 1.0$ mg/s that transitions to a cool diffusion flame (Test C).	37
Fig. B.5. Temporal plots of measurements for multiple hot-cool flame transitions at $\dot{m}_{HC} = 1.0$ mg/s (Tests F1-F5).....	38
Fig. C. 1. The contour of peak intensity with a circle and its radius in pixels for: (a) Test B, (b) Test C, (c) Test D, and (d) Test E.....	39
Fig. C.2. The contour of peak intensity with a circle and its radius in pixels for: (a) Test F1, (b) Test F2, (c) Test F3, (d) Test F4, (e) Test F5, and (f) Test G1.	40
Fig. C.3. The contour of peak intensity with a circle and its radius in pixels for: (a) Test G2, (b) Test G3, (c) Test G4, (d) Test G5, and (e) the spherical burner.....	41

Fig. D.1. Averaged image of the cool flame and a plot of the pixel values along the dashed line: (a) Test A and (b) Test B.	42
Fig. D.1. Averaged image of the cool flame and a plot of the pixel values along the dashed line: (a) Test A and (b) Test B.	42
Fig. D.2. Averaged image of the cool flame and a plot of the pixel values along the dashed line: (a) Test D and (b) Test E.	43
Fig. D.2. Averaged image of the cool flame and a plot of the pixel values along the dashed line: (a) Test D and (b) Test E.	43
Fig. D.3. Averaged image of the cool flame and a plot of the pixel values along the dashed line: (a) Test F1 and (b) Test F2.	43
Fig. D.3. Averaged image of the cool flame and a plot of the pixel values along the dashed line: (a) Test F1 and (b) Test F2.	43
Fig. D.4. Averaged image of the cool flame and a plot of the pixel values along the dashed line: (a) Test F3 and (b) Test F4.	44
Fig. D.4. Averaged image of the cool flame and a plot of the pixel values along the dashed line: (a) Test F3 and (b) Test F4.	44
Fig. D.5. Averaged image of the cool flame and a plot of the pixel values along the dashed line: (a) Test F5 and (b) Test G1.....	44
Fig. D.5. Averaged image of the cool flame and a plot of the pixel values along the dashed line: (a) Test F5 and (b) Test G1.....	44
Fig. D.6. Averaged image of the cool flame and a plot of the pixel values along the dashed line: (a) Test G2 and (b) Test G3.....	45

Fig. D.6. Averaged image of the cool flame and a plot of the pixel values along the dashed line: (a) Test G2 and (b) Test G3.....	45
Fig. D.7. Averaged image of the cool flame and a plot of the pixel values along the dashed line: (a) Test G4 and (b) Test G5.....	45

Chapter 1: Introduction

1.1 Background

Cool premixed flames were discovered in the 1800s. Initially thought to be only a novelty, their study increased dramatically when they were identified as responsible for knock in internal combustion engines [1,2]. Cool flames were characterized by their faint bluish luminescence and relatively low heat generation due to the reactions of fuel-oxidizer mixtures at low temperatures [3,4].

Cool diffusion flames were first observed only in the last decade. In these flames the fuel and oxidizer are supplied from opposite sides and arrive at the flame via diffusion, whereas in cool premixed flames the flames propagate into a premixture. The equivalence ratios and temperature distributions of the two flame types are so different that a full understanding of cool flame chemistry will require studies in both premixed and diffusion flames.

Cool flames are different from their hot flame counterparts in that: their peak temperatures are only 500 – 1000 K [5]; they increase the gas temperature by only 2 – 200 K [3]; they only consume a small fraction of the reactants; and they produce primarily H_2O , CO , H_2O_2 , CH_2O , and C_2H_4 [6], see also [1,7,8].

Cool flames are possible only under conditions with negative-temperature coefficients (NTCs) in the overall reaction rate. NTC regions are where the overall oxidation reaction rate decreases with the increase of temperature. Figure 1.1 shows an example of such NTC regions. Two NTC regions, (2) and (4), exist in a dibutyl-ether (DBE) oxidation in a jet-stirred reactor [9]. Within the NTC regions, an increase in the

peak temperature causes deceleration of the chemistry. Therefore, the rate of heat release decreases, and this consequently causes the peak temperatures to decrease. On the other hand, a temperature decrease causes the chemistry to increase the heat release rate, causing the temperature increases to its stable value. Such NTCs are near the crossover temperature, for which alkyl radicals are consumed at equal rates by cool and hot flame chemistry.

Cool flames are of practical interest because their low-temperature combustion (LTC) chemistry may contribute to the improvement of advanced high-efficiency engine technologies, such as homogeneous charge compression ignition (HCCI), premixed charge compression ignition (PCCI), and reactivity controlled compression ignition (RCCI) [2,10–13]. Due to the significantly high pressures in the mentioned engines, which is a favorable condition to cool flames, the LTC is likely to occur during

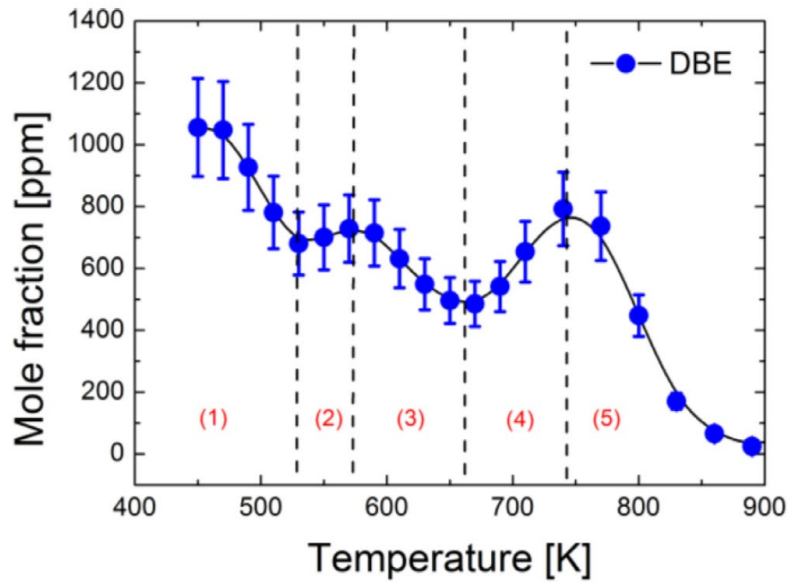


Fig. 1.1. Dibutyl-ether (DBE) mole fraction profile in jet-stirred reactor under fuel-rich conditions ($\phi=2$), at 10 atm and for $\tau = 700$ ms [9].

the combustion processes. Therefore, understanding of cool flames is necessary to improve engine performance and reduce emissions. In addition, hot flame chemistry is restrained in advanced engine technologies because of the considerable amounts of exhaust gas recirculation (EGR); therefore, cool flames become more prominent [2]. Figure 1.2 shows the two types of ignitions with different initial mixture temperatures of 700 K and 1000 K in a lean n-heptane/air mixture at 20 atm. At an initial temperature of 700 K, the LTC causes a first ignition followed by a subsequent hot flame ignition [2].

The LTC and two stage ignitions, transition from a cool flame ignition to a hot flame ignition, have been studied for fire and explosion prevention in aircraft fuel tanks because the conditions in aircraft fuel tanks, that are exposed to high temperatures and low pressures due to their high altitude, may cause ignition in the fuel tanks by cool

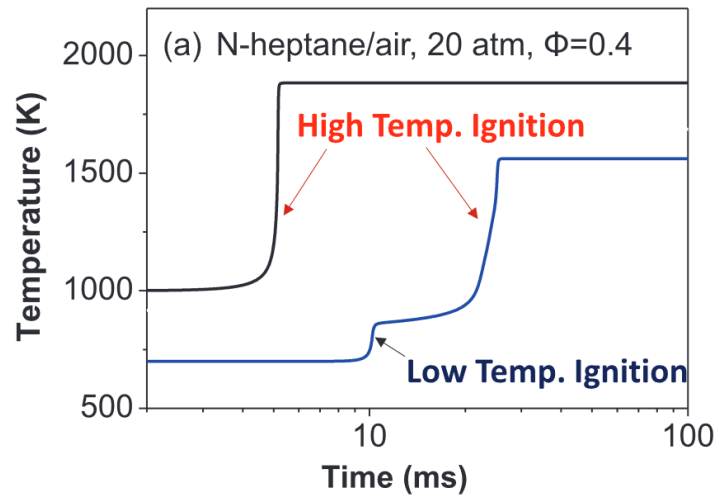


Fig. 1.2. Computed low temperature ignition and high temperature ignition of *n*-heptane/air mixtures by a kinetic model. Ignition temperature as a function of time at 20 atm and equivalent ratio of 0.4 at 700 K and 1000 K, respectively [2].

flame chemistry, hot flame chemistry, and/or two stage ignition chemistry [14,15]. An investigation into the explosion of Flight TWA in 1996, which claimed more than 200 lives, also concluded that a cool flame could be one of the possible ignition sources [16,17].

Cool diffusion flames were discovered in *n*-heptane droplet combustion experiments aboard the International Space Station (ISS) [7]. In Fig. 1.3, the square of the *n*-heptane droplet diameter decreases with time while the visible flame is observed. Surprisingly, after the hot flame is extinguished, the square of the droplet diameter continues to decrease at a constant rate, implying that the fuel is consumed by a cool flame [7]. Additional cool diffusion flames burning droplets in microgravity were observed for *n*-heptane, *n*-octane, *n*-decane, *n*-dodecane, and decane/hexanol mixtures

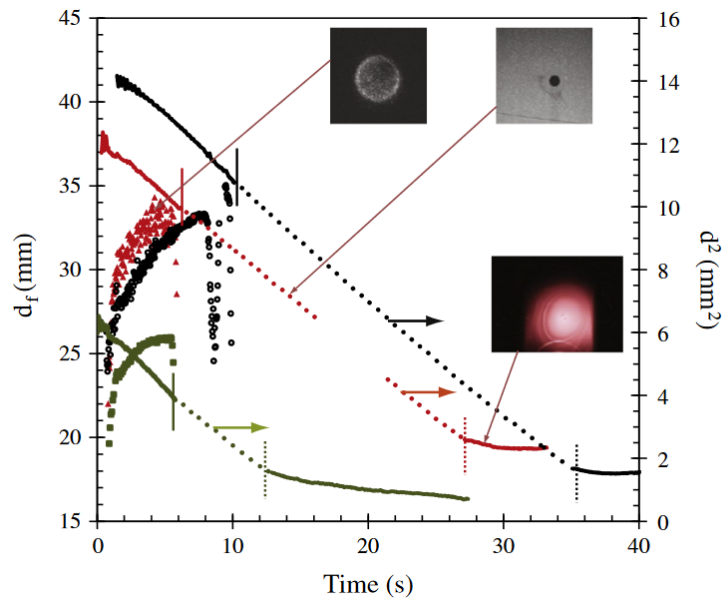


Fig. 1.3. Examples of radiative extinction and subsequent second-stage combustion of *n*-heptane droplets [7].

[18–21]. In most cases the cool diffusion flames appeared soon after the radiative extinction of a hot flame, but they were sometimes ignited directly by a resistively heated wire [2,13]. Some of the cool diffusion flames led to hot flame ignitions. The cool diffusion flames burned for up to 35 s before extinguishing [2,7,13]. Extensive modeling of these flames has been performed [8,13,20].

The existence of counterflow cool diffusion flames was predicted by Law and co-workers [10,22]. These flames were subsequently observed in normal gravity for *n*-butane, iso-butane, *n*-heptane, *n*-octane, *n*-decane, *n*-dodecane, *n*-tetradecane, dimethyl ether, and diethyl ether at various pressures [5,12,23–26]. Owing to the short residence times available in counterflow flames, they required LTC enhancements such as heated reactants, pulsed plasmas, and ozone addition [5,23]. Figure 1.4 shows an example of

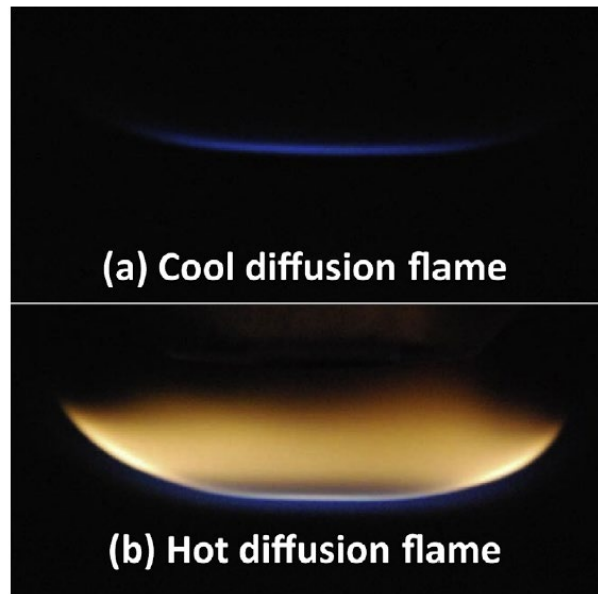


Fig. 1.4. Direct photos of cool (a) and hot (b) diffusion flames, observed at the identical flow condition, fuel mole fraction (X_f) = 0.07 and strain rate (a) = 100 s⁻¹ [5].

a cool diffusion flame observed in a counterflow burner with diluted *n*-heptane and pure oxygen [5].

Counterflow multistage warm diffusion flames, with peak temperatures around 1000 K, were discovered soon after [13,20,27,28]. These have been observed for *n*-heptane, *n*-decane, *n*-dodecane, and dibutyl ether.

Burner-supported spherical cool diffusion flames in normal gravity were observed and modeled by [29,30]. These involved dimethyl ether with diluents and pressures chosen to minimize gravitational interference.

Cool diffusion turbulent flames were investigated experimentally and numerically for dimethyl ether in a jet flame configuration [31]. Auto-ignition assisted turbulent cool diffusion flames were studied for diethyl ether in the same jet flame configuration [26].

1.2 Motivation and Objective

Despite extensive past work, gaps remain in the understanding of cool diffusion flames. Droplet studies cannot control or precisely measure the fuel supply rate or become fully steady. They also do not allow for fuel dilution, inverse flames, or gaseous fuels. Furthermore, their detailed models are complicated by the liquid phase. Counterflow flames cannot obtain the low strain rates and long residence times of spherical diffusion flames, have small length scales that complicate measurements, and require heated reactants, plasma, and/or ozone assistance. Normal gravity spherical diffusion flames are affected by buoyant entrainment, especially outside the flame. The

spherical cool diffusion flames studied here avoid these shortcomings. They are not perfect, however; for example, the support tube is a thermal mass that quenches the flames, and the burner temperature is not easily controlled.

Thus motivated, the objectives of this study are to use a spherical porous burner with gaseous fuels to observe spherical hot and cool diffusion flames in microgravity and to develop a simple model of these flames. Three alkane fuels are considered – ethane, propane, and *n*-butane – as are normal and inverse flames. A wide range of flow rates and nitrogen dilution of the fuel and oxidizer are studied at various pressures. The flame size measurements are compared with model predictions.

Chapter 2: Experiments

2.1 *Experimental Setup*

These experiments are part of the Cool Flames Investigation with Gases (CFI-G) project. The tests were performed aboard the ISS inside the Combustion Integrated Rack (CIR) using the Advanced Combustion via Microgravity Experiments (ACME) insert. The CIR includes avionics, gas containers, connections to vacuum and nitrogen, and interfaces for data uplink and downlink. A windowed pressure vessel with a free volume of 83 L, which was located at the center of the CIR, provided quiescent ambient conditions. The ACME insert provides mounting for various diagnostics, a spherical porous burner on the chamber axis, and a retracting resistive igniter. The chamber insert includes three mass flow controllers for the delivery of fuel, oxidizer, and nitrogen to the burner. The ACME insert is shown in Fig. 2.1.

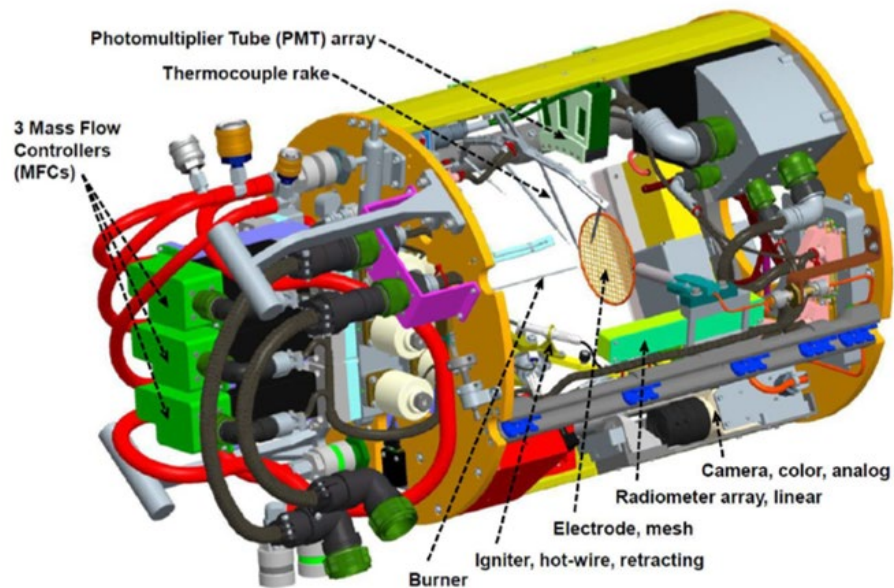


Fig. 2.1. Solid model representation of the ACME chamber insert [32].

A 6.4 mm diameter spherical porous burner, shown in Fig. 2.2, was located near the center of the pressure vessel. The burner was fabricated from sintering 316 stainless steel with 10-micron media grade, for which the porosity was approximately 41% and the density was 4.6 g/cm³. The burner was furthermore sinter-bonded to its stainless steel supply tube. To supplement the rigidity of the fuel supply tube, a close-fitting support tube, with an outer diameter of 1.8 mm, was added. The performance of the burner with its size and porosity was well verified by the work of [33].

The burner temperature was measured using a very fine type K (nickel/chromium/alumel) thermocouple, which was embedded as much as ~1 mm into the porous sphere surface. The location of the embedded thermocouple is shown in Fig. 2. Tests were terminated if the burner reached 723 K to prevent burner damage.

The retractable coil igniter, which was resistively heated, was used to start flames. It had an exchangeable tip and arm, and its stepper-motor drive enables precise positioning. The voltage level and duration of activation were controlled to provide appropriate ignition conditions for the tests.

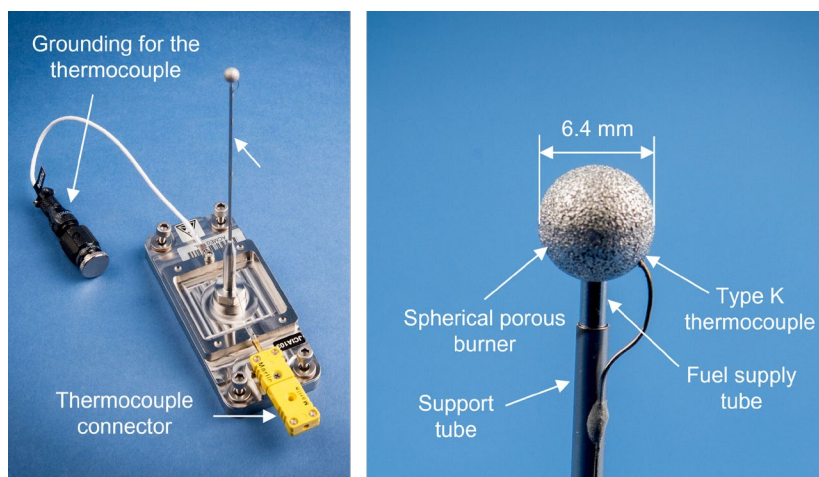


Fig. 2.2. The spherical porous burner and its assembly prior to testing [32].

Two types of diffusion flames were observed: normal flames, with the fuel flowing from the burner toward the oxidizer, and inverse flames, with the oxidizer flowing toward the fuel.

The fuels were ethane, propane, and *n*-butane, and they were generally diluted with N₂. For propane and *n*-butane inverse flames, the fuel supply was two-phase. The oxidizer was O₂, which was diluted with N₂. The nitrogen was available from the ISS, but the fuel and oxidizer supplies were transported from Earth to the ISS by spacecraft.

The chamber was filled with its target atmosphere prior to the burner gas flow. The burner gas flow rates were controlled with mass flow controllers with an approximated uncertainty of $\pm 5\%$. The gas delivery system enables dilution of the fuel or oxidizer flows by adding nitrogen flow. The ambient temperature was 298 K.

2.2 Diagnostics

Three different type of cameras were used to record images of the experiment. A standard analog camera mounted on the chamber insert was used to record and monitor the tests in real time at 30 frames/s (fps). The analog camera recordings were also downlinked in near real time to support the experiment operations.

A high-definition digital camera mounted outside of the chamber provided recordings at up to 30 fps with the resolution of 1360x1024 pixels. The zoom, iris, and focus of the camera was controlled by motorized lens. The digital camera was equipped with a blue-green filter, which balances the color planes to avoid saturation

in the red while maintaining sensitivity in the blue and green. The purpose of this filter was for thin filament pyrometry (TFP).

To image the low intensity of cool flames, a digital monochrome intensified camera was also used, at 23 fps with the resolution of 1392x1040 pixels. It had a bandpass filter of 390 – 490 nm to admit light from excited formaldehyde (CH_2O^*), which dominates the visible emissions from cool flames.

For some flames a type B (platinum/rhodium) thermocouple measured gas temperatures. This had a wire diameter of 0.2 mm and was at a radius of 13 mm.

Grayscale thin filament pyrometry (TFP) was performed with 14 μm diameter SiC fibers. The fibers were orthogonal to the flame axis and the array was translated along the flame axis to the predetermined position towards the burner. Figure 2.3 shows the glowing fibers in a flame and the fiber array. TFP analysis was conducted by using the method of Irace et al. [33].

The ACME chamber insert was also equipped with non-imaging optical diagnostics including thermopile radiometers and Photomultiplier Tubes (PMTs). A Schmidt-

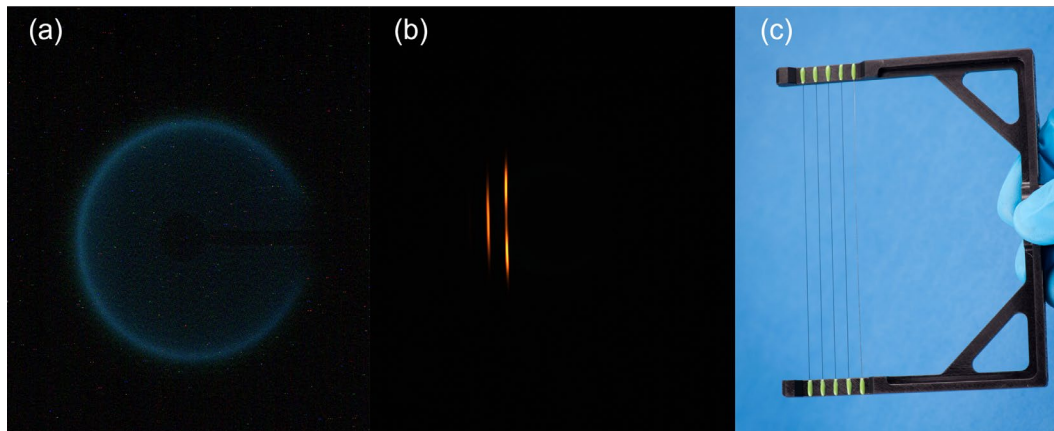


Fig. 2.3. Fibers used for TFP analysis: (a) hot flame image by the digital camera, (b) glowing fibers in a hot flame with the same conditions of (a), and (c) fiber array [32].

Boelter wide-angle thermopile radiometer measured radiative emissions. This was at a radius of 154 mm and was sensitive to wavelengths of 0.6 – 50 μm . Two other radiometers, at 0.2 – 17.5 μm , confirmed these measurements. They were mounted at distances of +60 mm, +30 mm and -10 mm from the assembly centerline. The Cool Flames Radiometer layout is shown in the Fig. 2.4.

Three wide-angle photomultiplier tubes (PMTs) measured optical emissions with bandpass filters of 230 – 700 nm for CH_2O^* , 310 nm for OH^* , and 430 nm for CH^* . However, these were only marginally able to detect the cool flames. A transducer measured chamber pressure. Additional details of the hardware and diagnostics are in [33,34], and the layout of the diagnostics is shown in Fig. 2.5.

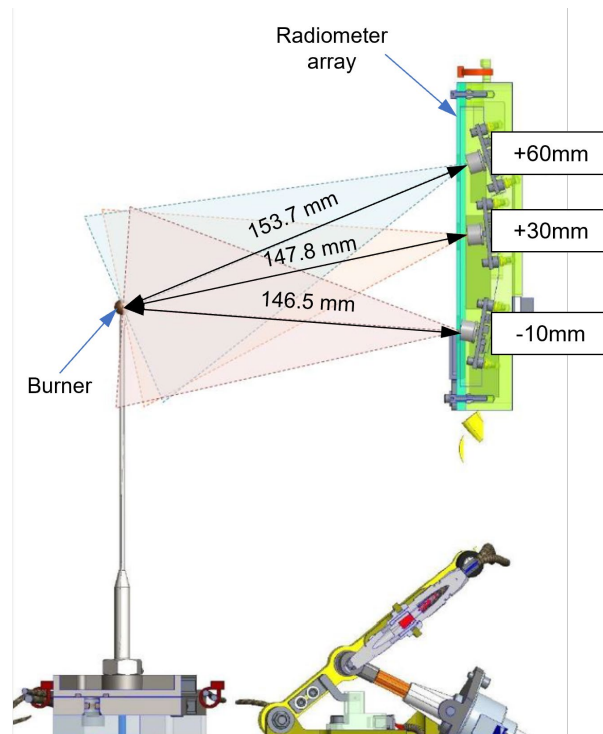


Fig. 2.4. Solid model representation of radiometer layout [32].

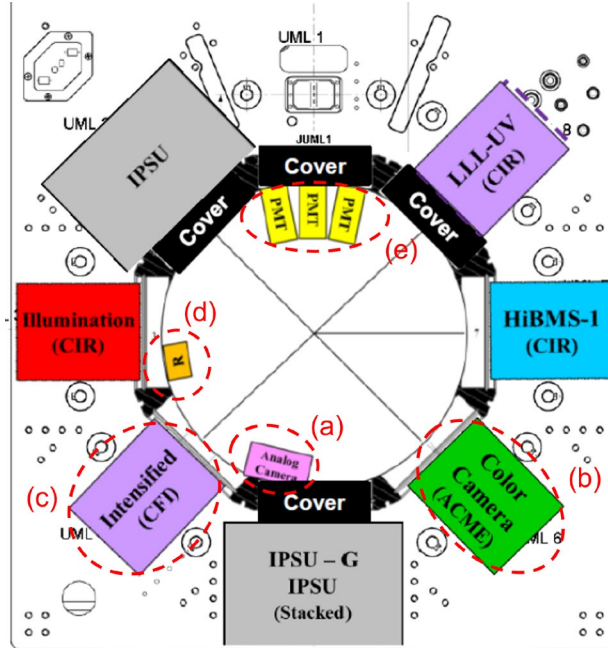


Fig. 2.5. Schematic layout of the ACME insert diagnostics (cross sectional view): (a) analog camera, (b) digital camera, (c) intensified camera, (d) radiometer array, and (e) PMTs [32].

2.3 Operation of Experiments

The configuration of experiments was conducted by the ISS crews, but the experiments were commanded from the ground from the Telescience Support Center (TSC) at the NASA Glenn Research Center in Cleveland, Ohio. Tests were performed in an automated mode using pre-programmed scripts. However, it was also possible to operate the experiments in a manual mode, where changes were made in response to the analog video downlink and the numerical data available in the command console at the TSC. For example, the intensified camera gain was increased from low to high manually by the operator while tests were running. This manual operation was to prevent the intensified camera with its high gain mode from being exposed to the excessive intensity of a flame, which could cause damage to the camera.

The operational sequence was as follows:

1. Preplan the test conditions, including the type of fuel, gas compositions, flow rates, chamber pressure, and parameters for diagnostics. TSC reviews the test conditions and finalizes the conditions.
2. TSC plans the required crew activities for the test. The CIR and ACME insert are configured by crew members.
3. On the test day, the chamber gas composition and pressure are established. Allow the chamber contents to reach equilibrium.
4. Take reference images and commence color imaging and monitoring measurements. After a few seconds, start the fluent flow, ignite the flame, and retract the ignitor.
5. By using the analog camera, monitor the test in real time. Observe the hot diffusion flame until radiative extinction occurs. Continuously record video and other measurements.
6. After radiative extinction, detect the possible presence of a cool diffusion flame while the fluent flow continues. Observe the cool diffusion flame until it extinguishes or transitions back to a hot diffusion flame.
7. Terminate the fluent flow. Record reference images. Terminate color imaging and monitoring measurements. Select data for downlink and downlink the data.

Chapter 3: Analytical

3.1 Normal Flames

Analytical models are derived here that relate the flame radii of burner-supported hot and cool diffusion flames to global parameters such as boundary temperatures, flow rates, and gas compositions.

The Spalding model of droplet burning [35] assumes: a quasi-steady fuel flow rate; unity Lewis number; constant product of density, ρ , and mass diffusivity, D ; uniform and constant pressure; and negligible radiation heat transfer. Although the spherical burner-supported flames are quasi-steady following the initial ignition transients, a similar model provided in [36] showed good agreement with measured flame diameters, and such assumptions have been used in many published analyses of microgravity droplet combustion [6–8,18–21,35,37–40]. In addition, radiation and unsteadiness are partially accounted for with our choice of appropriate transport rates, which is explained below.

Thus, this model is extended here to burner-supported hot diffusion flames, as in [33], and cool diffusion flames. Conservation of mass and mixture fraction become

$$\rho v r^2 = \rho_s v_s r_s^2, \quad (3.1)$$

and

$$\rho v r^2 \frac{dZ}{dr} = \frac{d}{dr} \left(r^2 \rho D \frac{dZ}{dr} \right), \quad (3.2)$$

where r is radius, s is the burner surface, v is velocity, and Z is mixture fraction.

An infinitely thin control volume at the burner surface, with inflow, outflow, and outward diffusion of Z , yields the burner boundary condition:

$$\rho_s v_s = \rho_s v_s Z_s - \rho_s D_s \left. \frac{dZ}{dr} \right|_s. \quad (3.3)$$

The first integration of Eq. (3.2) is facilitated with conservation of mass. Including the burner boundary condition ($1 \rightarrow Z$ as $0 \rightarrow r$) then yields

$$\frac{dZ}{dr} = \frac{-v}{D} (1 - Z). \quad (3.4)$$

Assuming constant ρD and using Eq. (3.1), Eq. (3.4) is readily integrated. The boundary condition at infinity for normal flames ($Z \rightarrow 0$ as $r \rightarrow \infty$) is then applied, yielding

$$\frac{v_s r_s^2}{D_s r} = \ln \left(\frac{1}{1 - Z} \right), \quad (3.5)$$

and

$$\frac{\dot{m}}{4 \pi \rho D r} = \ln \left(\frac{1}{1 - Z} \right), \quad (3.6)$$

where \dot{m} is the total mass flow rate from the burner.

Evaluating Eq. (3.6) at the porous burner surface yields the burner surface mixture fraction,

$$Z_s = 1 - \exp \left(\frac{-\dot{m}}{4 \pi r_s \rho D} \right). \quad (3.7)$$

The hot flame stabilizes at the stoichiometric mixture fraction, Z_{st} . Solving Eq. (3.6) at this location yields the hot flame radius for normal flames,

$$r_{hf} = \frac{\dot{m}}{4 \pi \rho D \ln \left(\frac{1}{1 - Z_{st}} \right)}, \quad (3.8)$$

Most cool diffusion flames do not reside at the stoichiometric location. Instead, their locations can be determined using temperature profiles in mixture fraction space as illustrated in Fig. 3.1. As discussed in [35], cool diffusion flames are in the partial-

burning regime, which requires dT / dZ to be opposite on the two sides of the flame.

For normal cool diffusion flames this can be expressed as

$$\frac{Z_{cf}}{Z_s - Z_{cf}} = \frac{T_{cf} - T_\infty}{T_{cf} - T_s}, \quad (3.9)$$

where subscripts cf , and ∞ denote the cool flame and the outer boundary. Rearranging yields

$$Z_{cf} = \frac{(T_{cf} - T_\infty) Z_s}{2 T_{cf} - T_s - T_\infty}. \quad (3.10)$$

This relationship, along with its analog for inverse flames, shows that for both flame types the burner surface and the ambient must be cooler than the cool flame.

Equations (3.1) – (3.7) are valid for both hot and cool flames, and it is shown below that a single ρD at room temperature can be used for both flames by evaluating the ρD at their respective flame temperatures. Therefore, Eq. (3.6) can be evaluated for normal cool diffusion flames at $Z = Z_{cf}$ and $r = r_{cf}$ to obtain

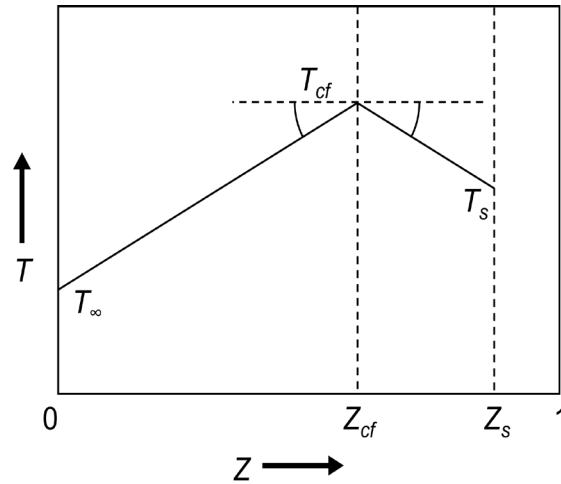


Fig. 3.1. Temperature T versus mixture fraction in the partial-burning regime for a normal cool diffusion flame, reproduced from Nayagam et al. [34].

$$r_{cf} = \frac{\dot{m}}{4 \pi \rho D \ln \left(\frac{1}{1 - Z_{cf}} \right)}, \quad (3.11)$$

with Z_{cf} given in Eq. (3.10). Finally, the ratio r_{hf} / r_{cf} is found from Eqs. (3.8), (3.10), and (3.11) to be

$$\frac{r_{hf}}{r_{cf}} = \frac{\ln (1 - Z_{cf})}{\ln (1 - Z_{st})} = \ln \left[1 - \frac{(T_{cf} - T_{\infty}) Z_s}{2 T_{cf} - T_s - T_{\infty}} \right] / \ln (1 - Z_{st}). \quad (3.12)$$

Equations (3.1) – (3.12) apply not only to burner-supported flames, but also to quasi-steady droplet flames.

Figure 3.2 plots the predictions of Eqs. (3.10) – (3.12) for Z_{cf} , r_{cf} , and r_{hf} / r_{cf} at conditions selected using experiments that are presented in the following section. When $T_s = T_{\infty}$ (here 300 K), quantities r_{cf} , Z_{cf} , and r_{hf} / r_{cf} barely depend on T_{cf} . For other

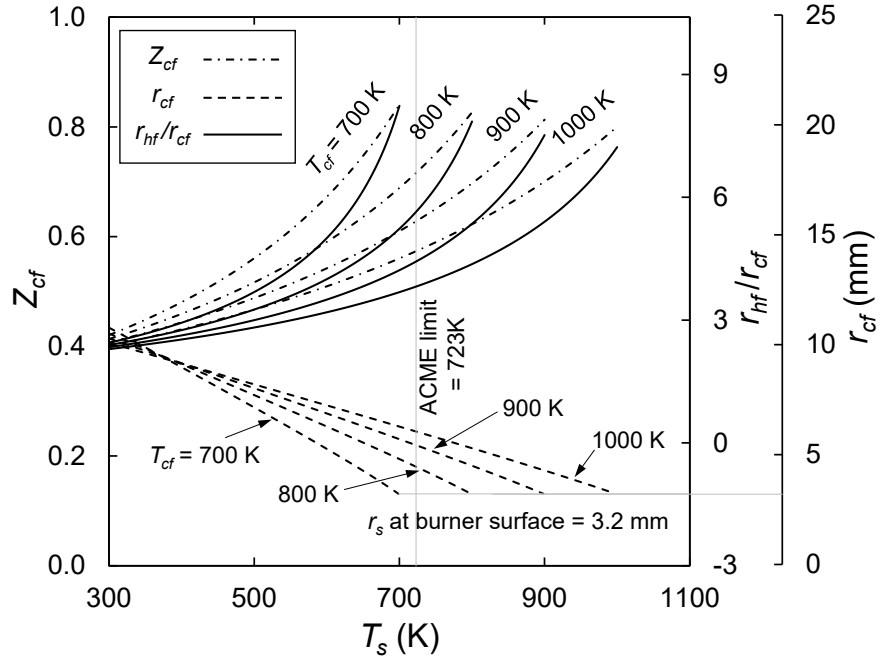


Fig. 3.2. Model predictions of normal cool diffusion flames for the conditions of $\dot{m}_{HC} = 1.5$ mg/s, $r_s = 3.2$ mm, $T_{\infty} = 300$ K, $Z_{st} = 0.20$, and $\rho D = 0.0334$ g/m-s at 300 K.

burner temperatures the cool flame size increases with T_{cf} . For increasing T_s , the cool flame shrinks monotonically until it collapses onto the burner when T_s reaches T_{cf} . The ACME burner temperature limit is indicated with a vertical line.

3.2 Inverse Flames

For inverse flames, Eq. (3.2) is integrated with the boundary conditions of inverse flames ($0 \rightarrow Z$ as $0 \rightarrow r$), which yields

$$\frac{dZ}{dr} = \frac{v}{D} Z. \quad (3.13)$$

Equation (3.13) is then integrated with the boundary condition at infinity ($Z \rightarrow 1$ as $r \rightarrow \infty$), yielding

$$\frac{v_s r_s^2}{D_s r} = \ln \left(\frac{1}{Z} \right). \quad (3.14)$$

Consequently, Eq. (3.6) and (3.7) are converted for inverse flames as below:

$$\frac{\dot{m}}{4 \pi \rho D r} = \ln \left(\frac{1}{Z} \right). \quad (3.15)$$

$$Z_s = \exp \left(\frac{-\dot{m}}{4 \pi r_s \rho D} \right). \quad (3.16)$$

Solving Eq. (3.15) at the stoichiometric location yields the inverse flame hot flame radius,

$$r_{hf} = \frac{\dot{m}}{4 \pi \rho D \ln \left(\frac{1}{Z_{st}} \right)}, \quad (3.17)$$

The corresponding temperature profile of an inverse cool diffusion flame is illustrated in Fig. 3.3.

The condition of partial burning regime addressed above can be expressed for inverse cool diffusion flames as

$$Z_{cf} = \frac{(T_{cf} - T_{\infty})Z_s + T_{cf} - T_s}{2T_{cf} - T_s - T_{\infty}}, \quad (3.18)$$

The radius of an inverse cool diffusion flame can be evaluated from Eq. (3.15) at $Z = Z_{cf}$ and $r = r_{cf}$ as,

$$r_{cf} = \frac{\dot{m}}{4\pi\rho D \ln\left(\frac{1}{Z_{cf}}\right)}, \quad (3.19)$$

with Z_{cf} given in Eq. (3.18). The ratio r_{hf}/r_{cf} for inverse flames from Eqs. (3.17) to (3.19) to be

$$\frac{r_{hf}}{r_{cf}} = \frac{\ln(Z_{cf})}{\ln(Z_{st})} = \ln\left[\frac{(T_{cf} - T_{\infty})Z_s + T_{cf} - T_s}{2T_{cf} - T_s - T_{\infty}}\right] / \ln(Z_{st}). \quad (3.20)$$

Figure 3.4 plots the predictions of Eqs. (3.18) – (3.20) for Z_{cf} , r_{cf} , and r_{hf}/r_{cf} at conditions with one inverse flame test point. When $T_s = T_{\infty}$ (here 300 K), quantities r_{cf} , Z_{cf} , and r_{hf}/r_{cf} barely depend on T_{cf} . For other burner temperatures the cool flame size increases with T_{cf} . For increasing T_s , the cool flame shrinks monotonically until it

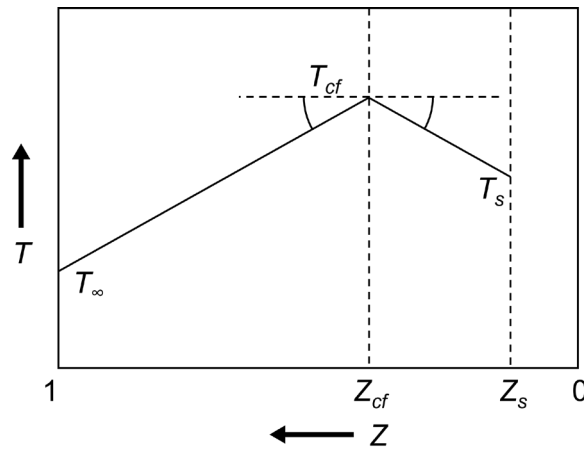


Fig. 3.3. Temperature T versus mixture fraction in the partial-burning regime for an inverse cool diffusion flame

collapses onto the burner when T_s reaches T_{cf} . The ACME burner temperature limit is indicated with a vertical line.

Equations (3.12), (3.17), and (3.19) show that, depending on the conditions, a normal or inverse cool flame can reside in rich or lean regions. When X_{O_2} is large, cool flames generally reside between the burner and the stoichiometric location.

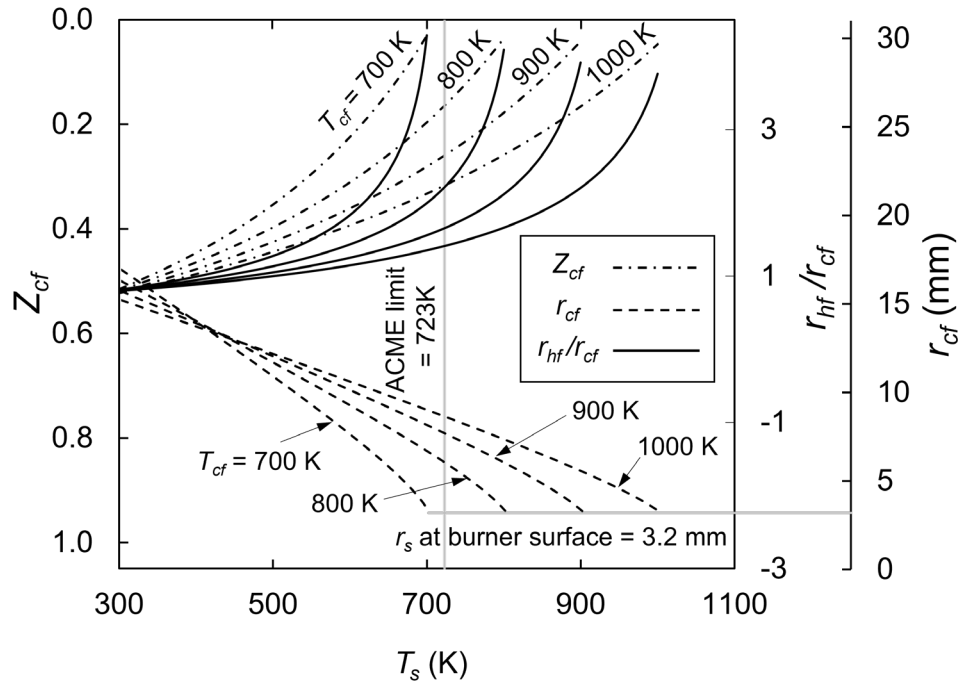


Fig. 3.4. Model predictions of inverse cool diffusion flames in the ambient filled with n -butane. The conditions are as follows: $\dot{m}_{O_2} = 5.37$ mg/s, $r_s = 3.2$ mm, $T_\infty = 300$ K, $Z_{st} = 0.44$, and $\rho D = 0.0334$ g/m-s at 300 K.

Chapter 4: Results and Discussion

4.1 Cool Flame Observation

A total of 280 hot diffusion flames were ignited. The temporal change of flame radius exhibited quasi-steady behavior as observed by Irace et al. in their similar flame experiments [36]. Among them, 189 extinguished radiatively and the others extinguished when the flow was terminated, in some cases because the burner temperature reached its limit of 723 K. A summary of the test conditions is provided in Table 4.1, where \dot{m}_{HC} and \dot{m}_{O_2} are the mass flow rates of hydrocarbon and O_2 , p is ambient pressure, and X is mole fraction. The uncertainty of ambient concentrations (X_{O_2} for normal flames and X_{HC} for inverse flames) was estimated to be $\pm 0.6\%$. The ambient temperature was 298 K. The test conditions were generally varied as widely

Table 4.1 Summary of the hot and cool flames observed.

Fuel	Flame type	X_{O_2}	X_{HC}	p (bar)	\dot{m}_{HC} or \dot{m}_{O_2} ^a (mg/s)	# of RE ^b	# of FT ^c	# of cool flames
ethane	Normal	0.18 - 0.4	0.25 - 1	0.51 - 2.03	0.50 - 2.36	30	10	0
propane ^d	Normal	0.21 - 0.4	0.05 - 1	0.94 - 3.04	0.13 - 2.89	34	6	0
<i>n</i> -butane	Normal	0.21 - 0.4	0.02 - 0.5	0.51 - 2.03	0.10 - 3.22	46	17	15
ethane	Inverse	0.12 - 0.85	0.06 - 0.3	0.46 - 3.04	0.93 - 9.08	25	22	0
propane	Inverse	0.18 - 0.85	0.08 - 0.43	0.51 - 3.04	1.36 - 9.07	24	13	0
<i>n</i> -butane	Inverse	0.21 - 0.85	0.06 - 0.36	0.51 - 3.04	1.34 - 8.95	30	23	0

^a \dot{m}_{HC} for normal flames and \dot{m}_{O_2} for inverse flames.

^b RE indicates radiatively extinguished.

^c FT indicates flow terminated.

^d For normal flames propane with X_{O_2} higher than 0.21 was only tested at $p \leq 1.01$ bar.

as permitted by safety requirements and the hardware. The changes to the ambient pressure, temperature, and concentrations were negligible during these tests.

When a flame extinguished radiatively, the flow was continued for at least 10 s to allow a possible transition to a cool diffusion flame. Despite the broad range of conditions, only 15 such cool flames ignited, as summarized in Table 4.2.

Table 4.2. Summary of the cool flames observed^a

Test ^{a, b}	\dot{m}_{HC} (mg/s)	cool flame duration (s)	r_{hf} (mm)	r_{cf} (mm)	r_{hf}/r_{cf}	Z_{cf}
A	0.75	14.3	12.4	5.1	2.4	0.43
B	1.0	13.8	14.6	5.3	2.8	0.51
C ^c	1.0	13.6	14.7	-	-	-
D	1.5	13.9	17.6	7.6	2.3	0.53
E	1.5	13.8	17.4	7.5	2.3	0.54
F1	1.0	6.2	14.4	5.1	2.8	0.55
F2	1.0	5.8	14.9	5.5	2.7	0.59
F3	1.0	5.5	14.7	5.7	2.6	0.60
F4	1.0	5.4	14.9	5.7	2.6	0.60
F5	1.0	5.3	14.4	5.5	2.6	0.60
G1	1.5	10.9	17.2	7.1	2.4	0.53
G2	1.5	3.4	17.3	6.5	2.7	0.50
G3	1.5	3.8	17.6	6.3	2.8	0.49
G4	1.5	4	17.6	6.2	2.8	0.49
G5	1.5	3.7	17.7	6.2	2.9	0.50

^a $X_{O_2} = 0.39$, $X_{HC} = 0.3$, $p = 2$ bar, n -butane normal flames, and $Z_{st} = 0.20$ for all tests. The adiabatic flame temperature was 2650 K.

^b Numbered tests involved hot-cool-hot flame transitions.

^c The cool flame radius for Test C could not be measured owing to low camera gain.

4.2 *Images of Cool Flames*

The cool flames were imaged only by the intensified camera because of the low flame temperatures, except during Test C. Figure 4.1 shows temporal changes of a flame, from ignition to extinction. The flame was first ignited ($t = 0$ s), gradually grew, and oscillated ($t = 82.6$ s). After the oscillation, the flame was radiatively extinguished. A second later, a cool flame appeared ($t = 88.0$ s), and it sustained till the fuel flow was terminated. The intensity of the hot flame decreased with time because the flame temperature decreased. The flames in the images at $t = 66.2$ s and 82.6 s are brighter than the images taken before because the gain of the intensified camera was increased to the maximum value to capture the dimmer flames. Although the gain of intensified camera was increased to the maximum value, the cool flames were barely visible in the images. Thus, the intensity of images was increased by a factor of 50, and the median filtering was applied to decrease the noise ($t \geq 87.5$ s).

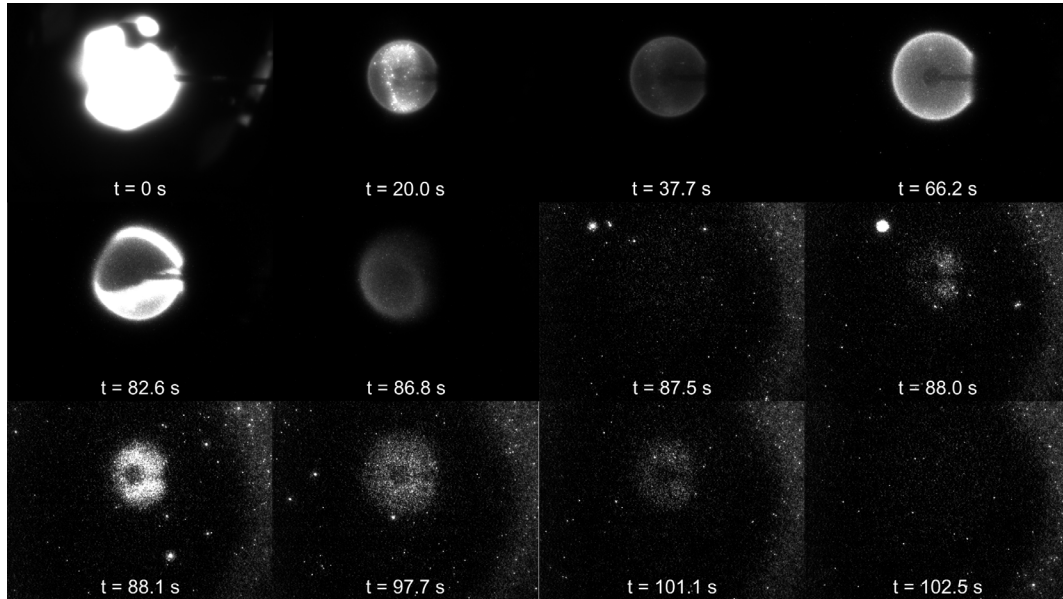


Fig. 4.1. Sequential intensified camera images of Test D, from the ignition to the extinction.

Figure 4.2 shows a hot flame 10 s before its radiative extinction and the subsequent cool flame. Compared to the cool flame, the hot flame was larger, brighter, and more spherical and it had a thinner reaction zone. The hot flame also had a larger quenched region near the cold burner support tube. Also, the flame was slightly shifted towards the burner support tube due to gas leakage at the supply tube connection to the porous sphere. However, given the good agreement on flame size between the numerical model and the measurements presented in [36], the influence of the support tube on the properties of the flames appeared negligible.

When each hot flame extinguished, the type B thermocouple was then in a rich premixture and catalyzed exothermic reactions [41] that reignited the hot flame. These reignitions occurred for Tests F and G when the thermocouple reached 720 – 820 K

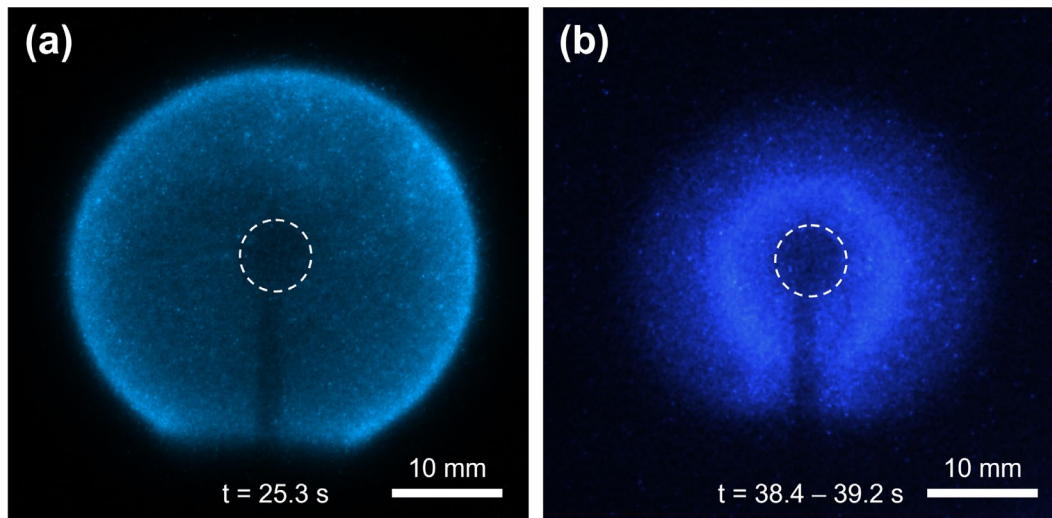


Fig. 4.2. Intensified camera images from Test D of (a) the hot flame and (b) the cool flame. The false colors here were obtained by matching the colors of microgravity hot flames and normal gravity cool flames. The times after ignition, t , are shown. The dashed circles indicate the burner location. Image (b) is an average of images from the times shown and has an exposure 50 times as bright as that of (a).

and were confirmed by the intensified camera as shown in Fig. 4.3. These were also confirmed by the radiometer signals and burner temperatures.

Thin filament pyrometry was attempted only for Test C. (This precluded using the high gain in the intensified camera for this test.) No glow was detected in the filament, indicating the peak temperature was below the TFP detection limit of 950 K, which is consistent with a cool diffusion flame, but not with a hot flame.

4.3 Radiometer Readings on Cool Flames

All three radiometers could detect the cool flames. Figure 4.4(a) shows the radiometer signal, burner temperature, and burner flow rate for a representative normal flame undergoing radiative extinction without a cool flame. Flame oscillations began at 18 s and increased in strength until flame extinction at 30 s. The flow continued for an additional 14 s, but no cool flame appeared in the intensified camera and the radiometer output followed an asymptote toward zero as the gas and burner cooled.

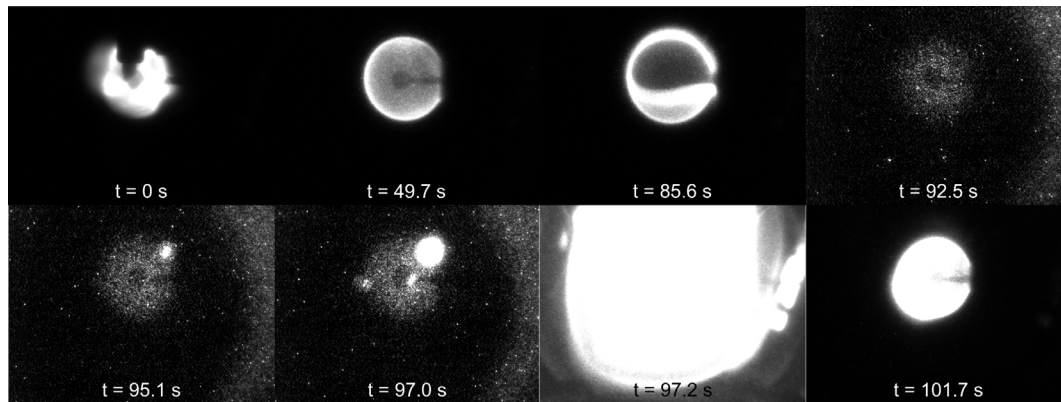


Fig. 4.3. Sequential intensified camera images of Test F. The flame was ignited ($t = 0$ s) and transitioned to a cool flame after oscillations ($t = 92.5$ s). The glow due to the type B thermocouple was growing as time increased, and reignited a hot flame ($t = 97.2$ s).

Figure 4.4(b) plots the same quantities for Test D. The conditions were the same as in Fig. 4.4(a) except for the decreased flow rate. The smaller flame and the longer hot-flame burn time increased the burner temperature at the time of radiative extinction. This occurred at 36 s and a cool diffusion flame appeared at 37 s. (A similar delay, 0.7 – 1.1 s, occurred for all 15 cool flames.) The fuel flow was terminated at 50 s, whereby the cool flame extinguished. During the cool flame, the radiometer output and burner

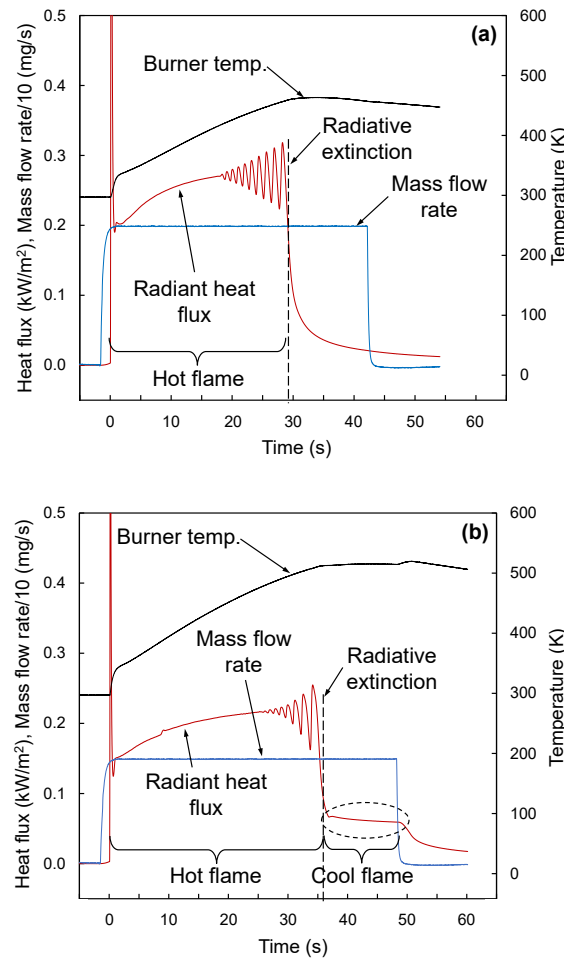


Fig. 4.4. Temporal plots of measurements for (a) a hot flame at $\dot{m}_{HC} = 2$ mg/s that extinguishes and (b) a hot flame at $\dot{m}_{HC} = 1.5$ mg/s that transitions to a cool diffusion flame (Test D).

temperature were steady enough to suggest this flame would have lasted indefinitely with continued flow and an infinite domain.

The cool flames in Tests A – E were not detected in real time because the intensified camera images and the radiometer output were not available until later. Therefore, their flows were terminated prematurely. This was remedied prior to Tests F and G. At the same time the type B thermocouple was added, as required for a different ACME project.

Figure 4.5 plots the same measurements for Tests G1 – G5. (These conditions are the same as those of Test D except for the addition of the type B thermocouple.) Here the hot flame radiatively extinguished at 40 s and a cool flame appeared at 42 s. However, the cool flame transitioned to a hot flame at 54 s owing to the presence of the type B thermocouple. Five such cool flames, preceded and followed by hot flames, were observed until the flow was terminated at 165 s. The first hot and cool flames

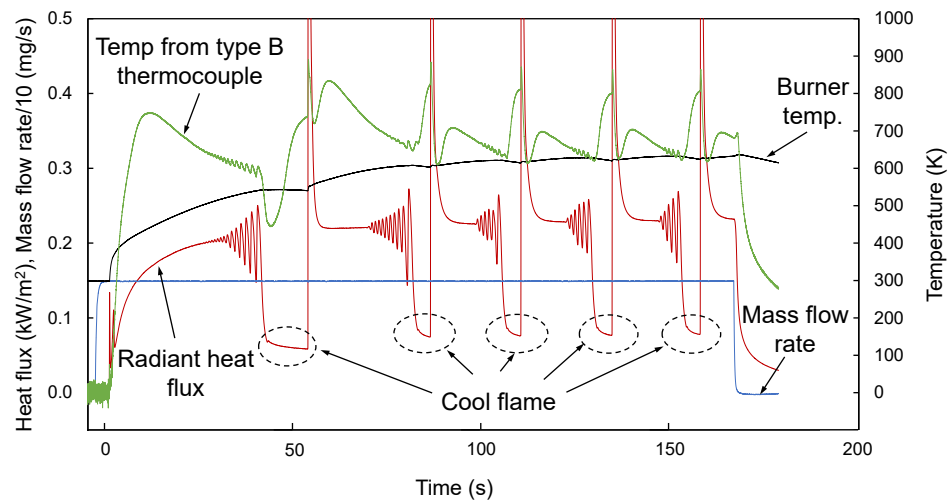


Fig. 4.5. Temporal plots of measurements for multiple hot-cool flame transitions at $\dot{m}_{HC} = 1.5 \text{ mg/s}$ (Tests G1-G5).

lasted longer than the others. As mentioned above, during each cool flame the type B thermocouple warmed and began to glow as shown in Fig. 4.5. . These temperatures have not been corrected for radiative loss or catalysis because the radiation corrections are small at these temperatures, catalytic corrections are highly approximate, and the thermocouple readings are more qualitative than quantitative.

4.4 *Hot and Cool Flame Size*

The intensified camera images were used to find flame radii for the tests of Table 4.2. The uncertainty of flame radii is estimated at $\pm 2\%$. As presented in [33], the hot flames supported by a spherical porous burner grow in size over time, and the size growth rate decreases and approaches to nearly zero. This asymptotic behavior of the hot flame size is also confirmed by the hot flame images and the radiometer signals (Fig. 4.4(a) and (b)). Since the analytical model discussed in the previous chapter assumes quasi-steady spherical hot flames, hot flame images just prior to oscillations, where the flames were assumably closest to the steady-state in the given burning conditions, were analyzed by fitting the contour of peak intensity with a circle.

The spherical burner in images was used as a reference object with a known length to convert the pixels to the length. The radius of flames was found by a Hough transform based algorithm [42] using a commercial software package MATLAB (R2021a) as shown in Fig. 4.6.

The cool flame locations could not be found by the mentioned MATLAB algorithm because the cool flames did not have a thin reaction zone. However, it can be

approximated that the cool flame is located in the middle of the NTC region, where the temperature is at its maximum (crossover temperature) [6,35]. Therefore, the pixel values of cool flame images were evaluated to identify the location at the crossover temperature.

The intensity of cool flame images was increased, and averaging and filtering were followed to reduce noise. Figure 4.7 shows the resulting image for Test G1. Pixel values along a line through the burner center and perpendicular to the support tube identified two peaks, as plotted in Fig. 4.7. The cool flame radius was found as half their separation distance, as was done by [35] for droplet flames.

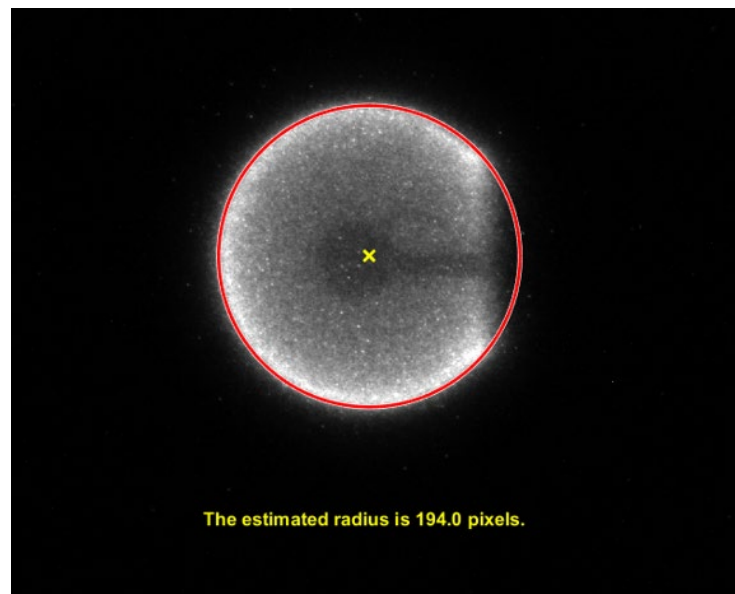


Fig. 4.6. The contour of peak intensity with a circle and its radius in pixels for Test A found by using a MATLAB algorithm.

The measured flame radii are shown in Table 4.2. The mean measured r_{hf} / r_{cf} is 2.6 and the mean predicted by Eq. (3.12) is 3.2 with appropriately selected ρD values, which are explained in the following paragraphs. Measurements from [19,35] for *n*-decane droplets indicate hot and cool flame standoff ratios of 8 and 3.2, i.e., $r_{hf} / r_{cf} = 2.5$. The model of [43] predicts this ratio to be 3 for an *n*-heptane droplet.

Figure 4.8 plots the measured versus modeled hot and cool flame radii. Cool flames of Table 4.2 are included, and normal *n*-butane hot flames for various conditions of

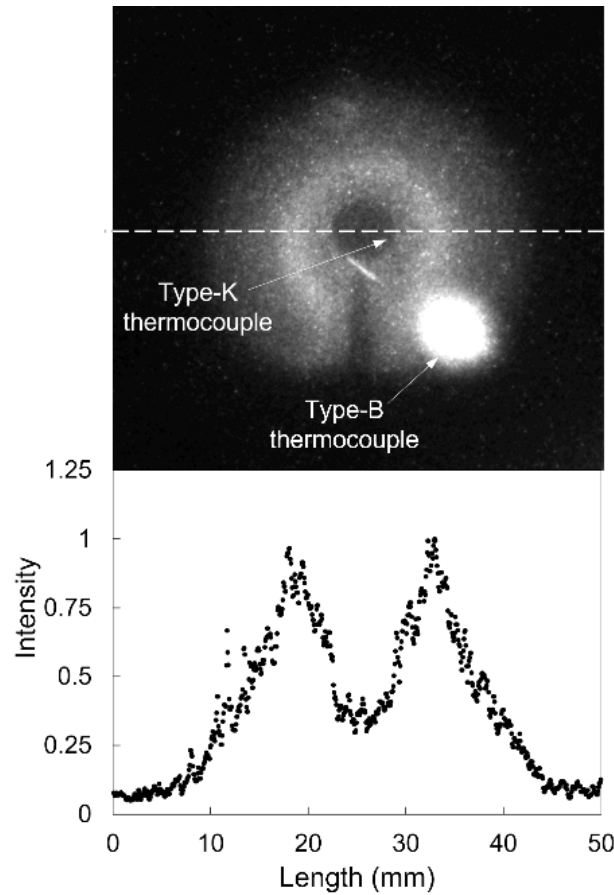


Fig. 4.7. Averaged image of the cool flame of Test G1 and a plot of the pixel values along the dashed line. The white streak in front of the burner tube is the type B thermocouple's double reflection off the camera lens and the window.

X_{O_2} (0.37 – 0.40), X_{HC} (0.15 and 0.3), \dot{m}_{HC} (0.75 – 2.0 mg/s), and pressure (0.5, 1, and 2 bar). The modeled radii are from Eqs. (3.8) and (3.11). A peak cool flame temperature of 750 K is assumed, which is reasonable for alkanes [2,7,8,13,20,39,44]. The respective flame temperatures, 1400 K for hot flames [36] and 750 K for cool flames, were considered to find a fitting constant in the model, ρD , at room temperature. Using the data of Fig. 4.8, it was optimized to a value of 0.0334 g/m-s. This value is assumed here to be constant for all hot and cool flames regardless of species. Wang et al. [45] found $\rho D = 0.0248$ g/m-s at 298 K for an equimolar mixture of O_2 and N_2 at 1.01 bar and 298 K. The present hot flames were smaller than their steady-state counterparts, and accounting for this would increase this ρD .

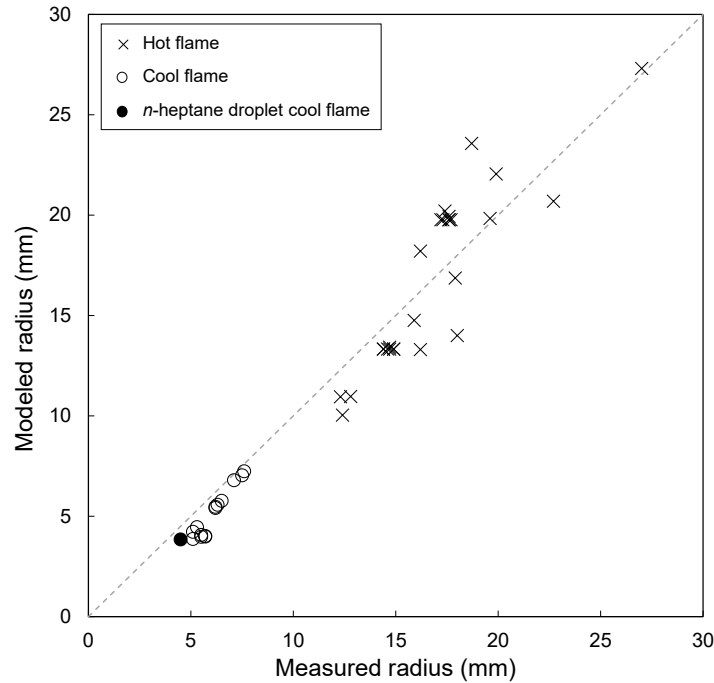


Fig. 4.8. Measured versus modeled flame radii for hot and cool flames. The droplet cool flame is from [34]. The data has a coefficient of determination of $R^2 = 0.92$ with respect to the line shown with unity slope.

Figure 4.8 indicates that the measured radii agree with the correlation within uncertainties in the measurements and model; thus, this model with $\rho D = 0.0334$ g/m-s at 300 K is reasonably successful in predicting hot and cool diffusion flame radii for these conditions. Equation (3.7) from the model indicates the mean Z_s for the cool flames of Table 4.2 is 0.75. The mean Z_{cf} is then found to be 0.53 from Eq. (3.11) and the measured radii. Finally, the mean T_{cf} is found from Eq. (3.10) to be 869 K. This temperature is higher than expected but is reasonable given the assumptions in the model.

4.5 Conditions for Cool Flames

As indicated by Tables 4.1 and 4.2, these cool diffusion flames are only possible for very limited conditions. For example, cool diffusion flames were not observed for ethane or propane, nor at pressures below 2 bar. This is consistent with the understanding that higher alkanes [46] and higher pressures [2,12] favor cool flames.

Cool flames were not observed for inverse burning, primarily owing to short residence times. The inverse flames also had low burner temperatures (below 500 K), but droplet cool diffusion flames are observed with surface temperatures near 400 K.

Cool flames were not observed for oxygen mole fractions below 0.4, which is consistent with a limiting oxygen index for cool flames [47]. Cool flames were not seen for fuel mole fractions other than 0.3, \dot{m}_{HC} outside the range of 0.75 – 1.5 mg/s, or when the burner was cooler than 515 K.

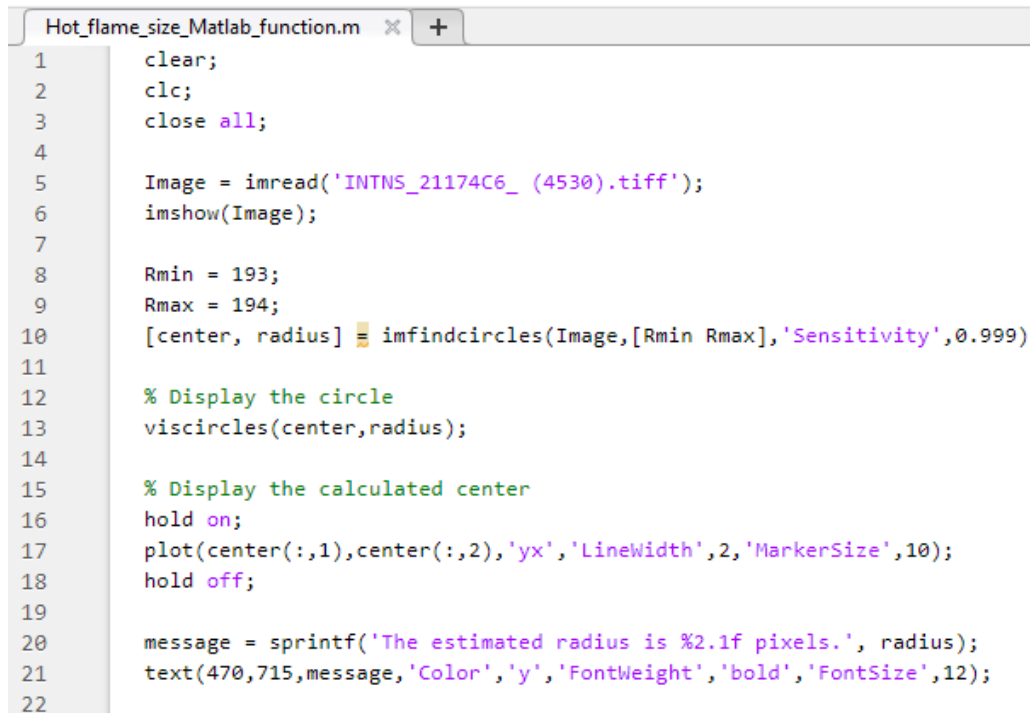
Chapter 5: Conclusions

Spherical diffusion flames burning gases were investigated aboard the ISS, seeking conditions suitable for cool diffusion flames. An analytical model of flame radii was formulated for hot and cool flames. The main conclusions are as follows.

1. Spherical cool diffusion flames burning gases were observed for the first time. Fifteen such flames were observed. They formed after the hot flames radiatively extinguished and they were quasi-steady until the flow was terminated. When a type B thermocouple was present, the cool flames transitioned to hot flames, leading to cyclic hot and cool flames.
2. Cool diffusion flames for these fuels are not easily obtained. They were only observed for normal *n*-butane flames at 2 bar in 39% O₂, and only for butane flow rates of 0.75 – 1.5 mg/s. In addition, these cool flames were only observed for burner temperatures in excess of 515 K.
3. The cool diffusion flames are smaller than their hot flame counterparts, with a mean ratio of hot/cool flame radii of 2.6.
4. The cool flame peak temperatures were below the TFP detection limit of 950 K.
5. The analytical model, based on the Spalding model of droplet combustion and the partial-burning regime, reveals quantitatively the importance of burner temperature on the size and peak temperatures of cool diffusion flames.
6. The model indicates that a reasonable approximation for ρD for these hot and cool flames is $\rho D = 0.0334$ g/m-s at 300 K. The model also indicates that these cool flames reside in rich regions with a mixture fraction of 0.53, and that their surface mixture fraction is 0.75.

Appendix A. MATLAB Code for the Flame Size Estimation

MATLAB provides a function “imfindcircles” to find circles in an image using the circular Hough transform. An intensified camera image in a TIFF format showing a hot flame was imported into an array with a size of 1040 x 1392 in 16-bit. Object polarity was set to “bright” to find a bright circle in darker background and “dark” in vice versa. The radius range (the minimum and maximum) was given to find a circle corresponding to the hot flame in the image only within the range. By iteratively adjusting the radius range and the sensitivity, a circle could be found satisfying the one-pixel width range and the sensitivity of 0.999. The burner size was found by applying the “dark” argument of the function. An example of the code is provided in Fig. A.1.

A screenshot of a MATLAB script editor window titled 'Hot_flame_size_Matlab_function.m'. The script contains 22 lines of code. Lines 1-3 are initialization commands: 'clear;', 'clc;', and 'close all;'. Line 5 reads an image 'INTNS_21174C6_ (4530).tiff' and displays it with 'imshow(Image);'. Lines 8-9 set radius bounds 'Rmin = 193;' and 'Rmax = 194;'. Line 10 uses 'imfindcircles' with sensitivity 0.999 to find the circle. Lines 12-13 display the circle with 'viscircles'. Lines 15-18 display the center with 'plot' and 'hold on/off'. Lines 20-21 format and display the estimated radius message. Line 22 is a blank line.

```
1 clear;
2 clc;
3 close all;
4
5 Image = imread('INTNS_21174C6_ (4530).tiff');
6 imshow(Image);
7
8 Rmin = 193;
9 Rmax = 194;
10 [center, radius] = imfindcircles(Image,[Rmin Rmax], 'Sensitivity',0.999)
11
12 % Display the circle
13 viscircles(center,radius);
14
15 % Display the calculated center
16 hold on;
17 plot(center(:,1),center(:,2),'yx','LineWidth',2,'MarkerSize',10);
18 hold off;
19
20 message = sprintf('The estimated radius is %2.1f pixels.', radius);
21 text(470,715,message, 'Color', 'y', 'FontWeight', 'bold', 'FontSize',12);
22
```

Fig. A.1. MATLAB code for the flame size estimation

Appendix B. Plots of Measurements with Tim

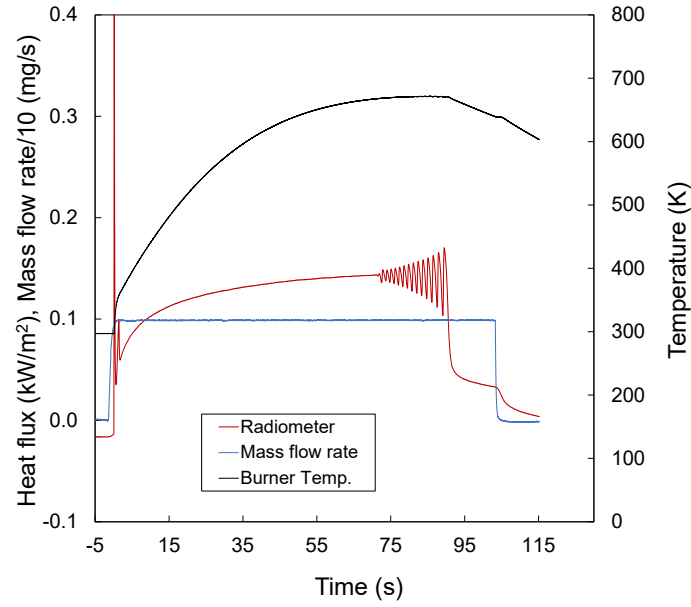


Fig. B.1 Temporal plots of measurements for a hot flame at $\dot{m}_{HC} = 1.0$ mg/s that transitions to a cool diffusion flame (Test B).

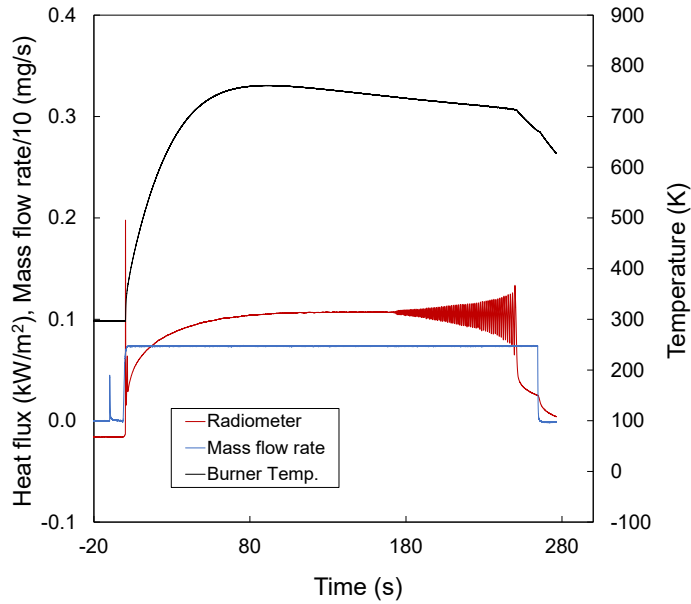


Fig. B.2. Temporal plots of measurements for a hot flame at $\dot{m}_{HC} = 0.75$ mg/s that transitions to a cool diffusion flame (Test A).

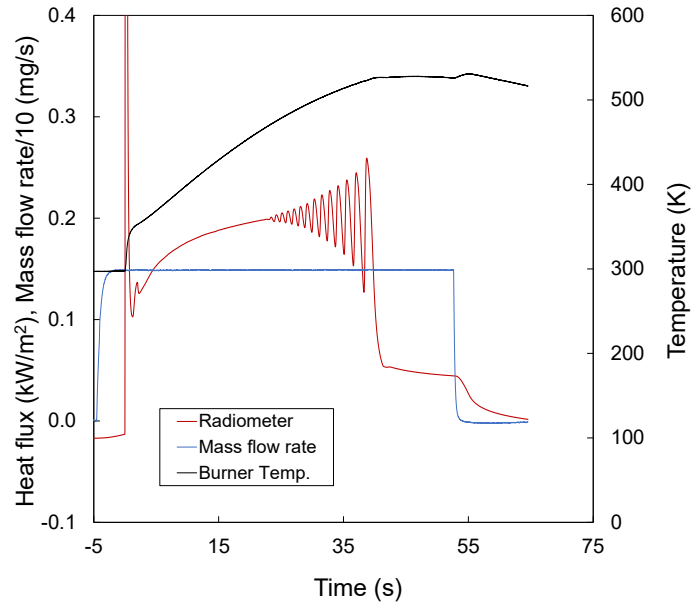


Fig. B.3. Temporal plots of measurements for a hot flame at $\dot{m}_{HC} = 1.0$ mg/s that transitions to a cool diffusion flame (Test E).

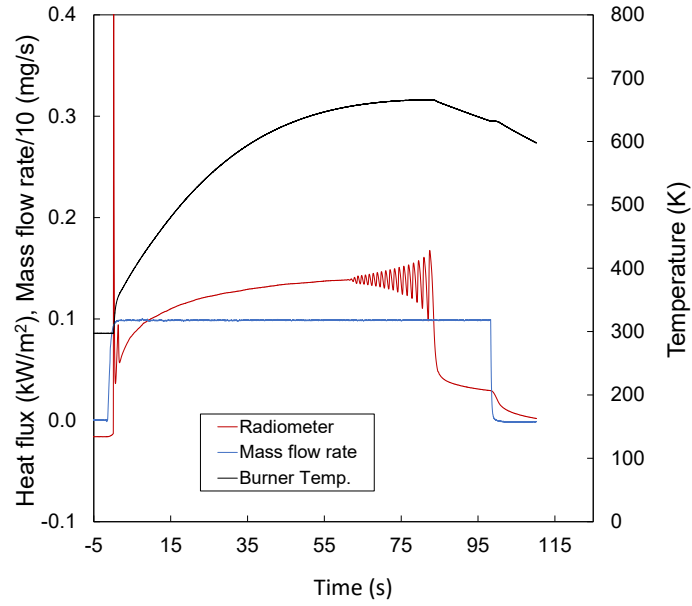


Fig. B.4. Temporal plots of measurements for a hot flame at $\dot{m}_{HC} = 1.0$ mg/s that transitions to a cool diffusion flame (Test C).

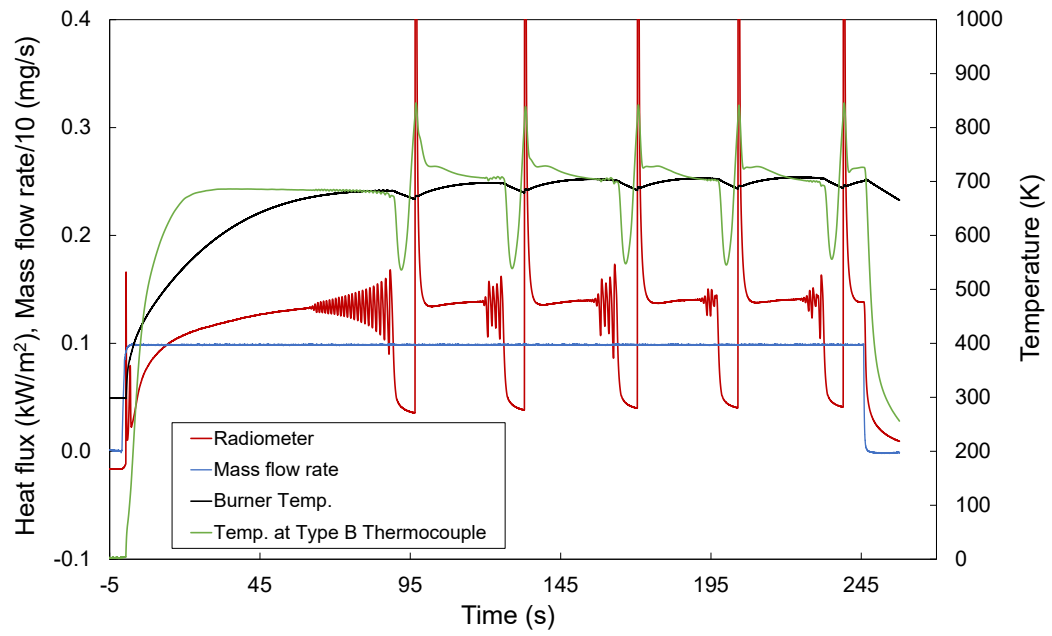


Fig. B.5. Temporal plots of measurements for multiple hot-cool flame transitions at $\dot{m}_{HC} = 1.0$ mg/s (Tests F1-F5).

Appendix C. Hot Flame Images and Their Size by Fitting the Contour of Peak Intensity with a Circle

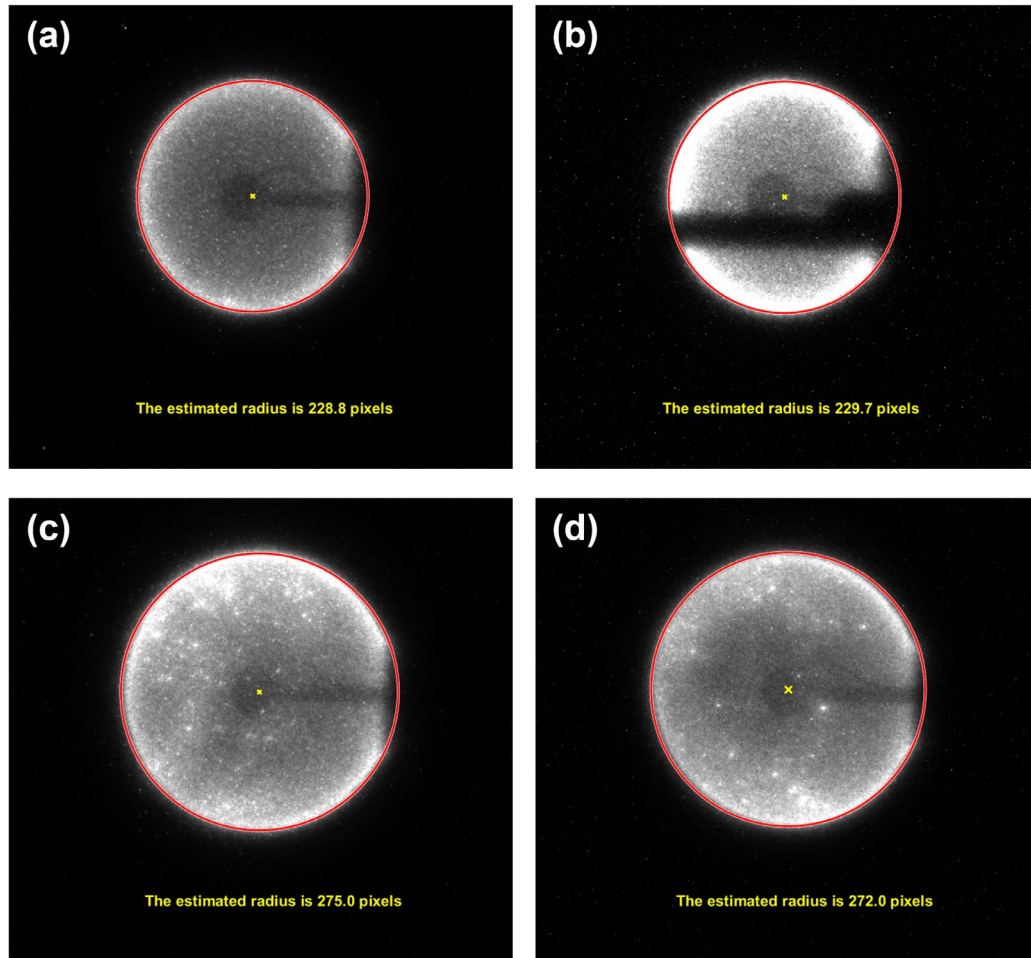


Fig. C. 1. The contour of peak intensity with a circle and its radius in pixels for: (a) Test B, (b) Test C, (c) Test D, and (d) Test E.

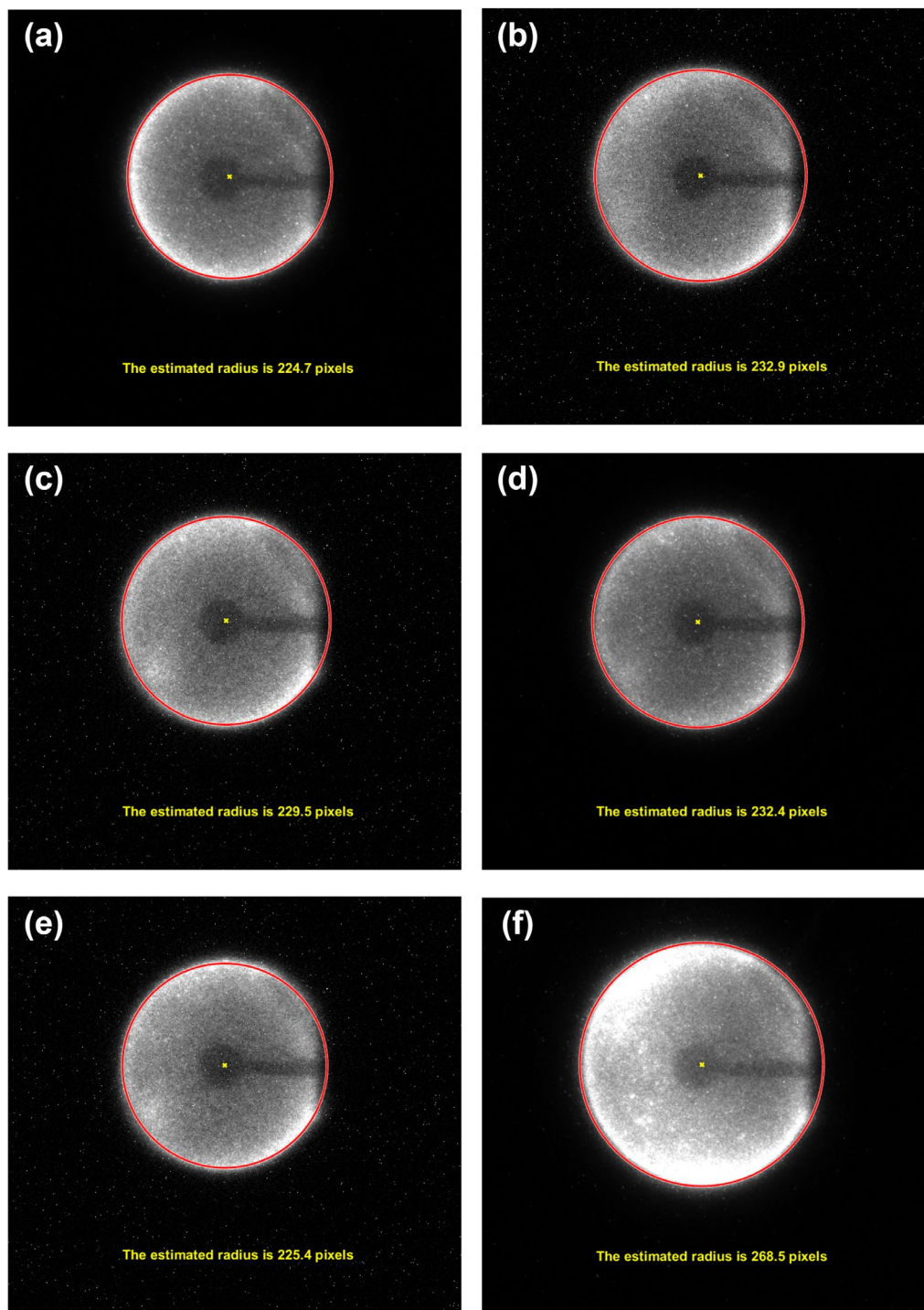


Fig. C.2. The contour of peak intensity with a circle and its radius in pixels for: (a) Test F1, (b) Test F2, (c) Test F3, (d) Test F4, (e) Test F5, and (f) Test G1.

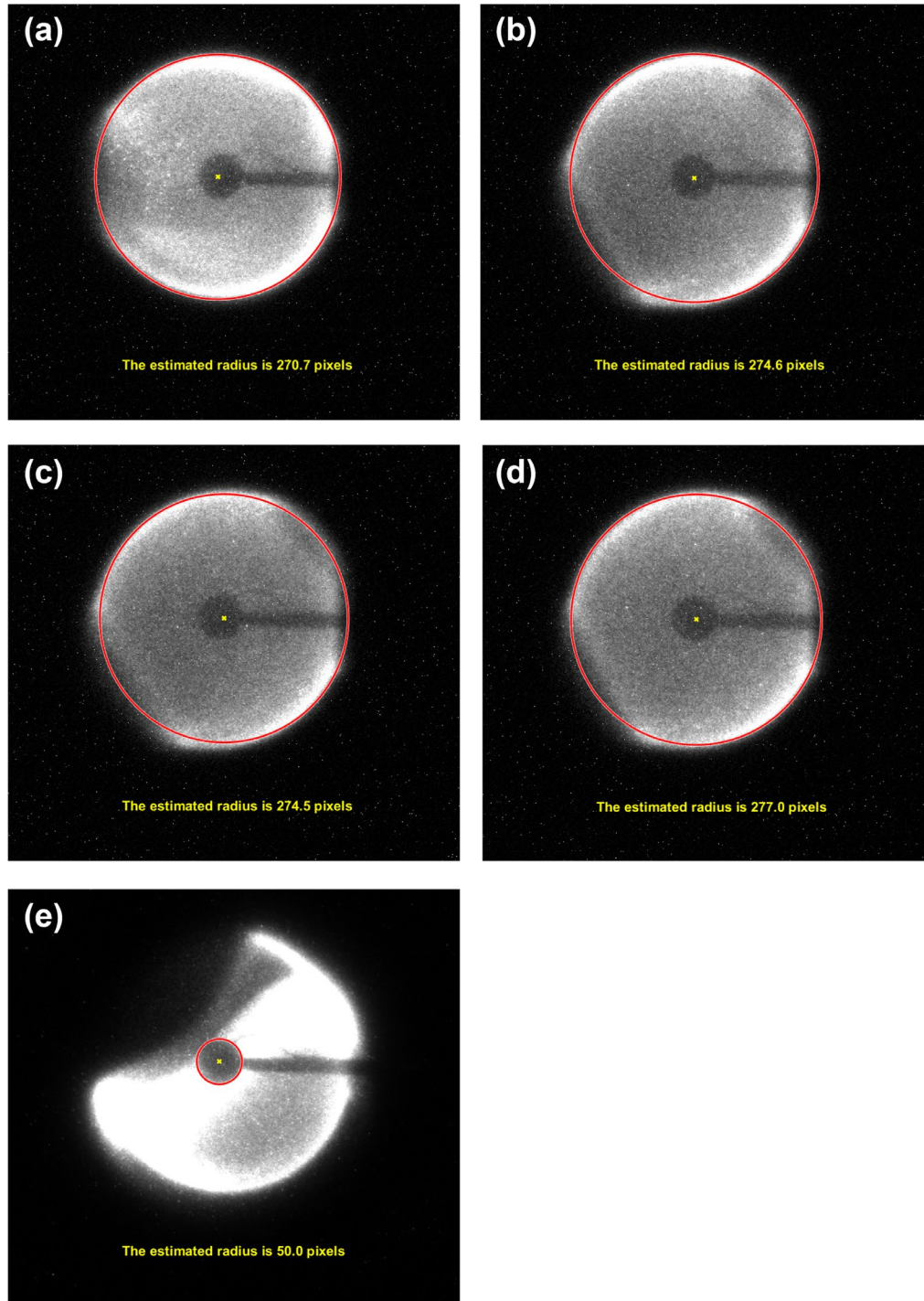


Fig. C.3. The contour of peak intensity with a circle and its radius in pixels for: (a) Test G2, (b) Test G3, (c) Test G4, (d) Test G5, and (e) the spherical burner.

Appendix D. Cool Flame Images and Distance between Two Peaks

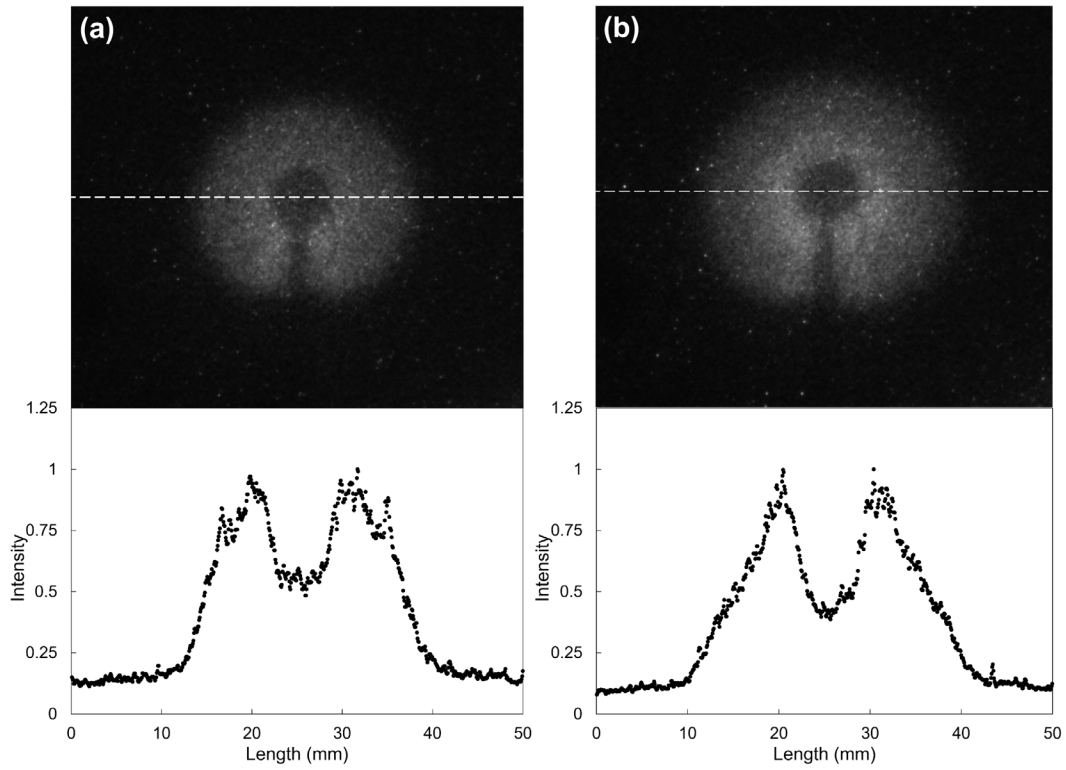


Fig. D.1. Averaged image of the cool flame and a plot of the pixel values along the dashed line: (a) Test A and (b) Test B.

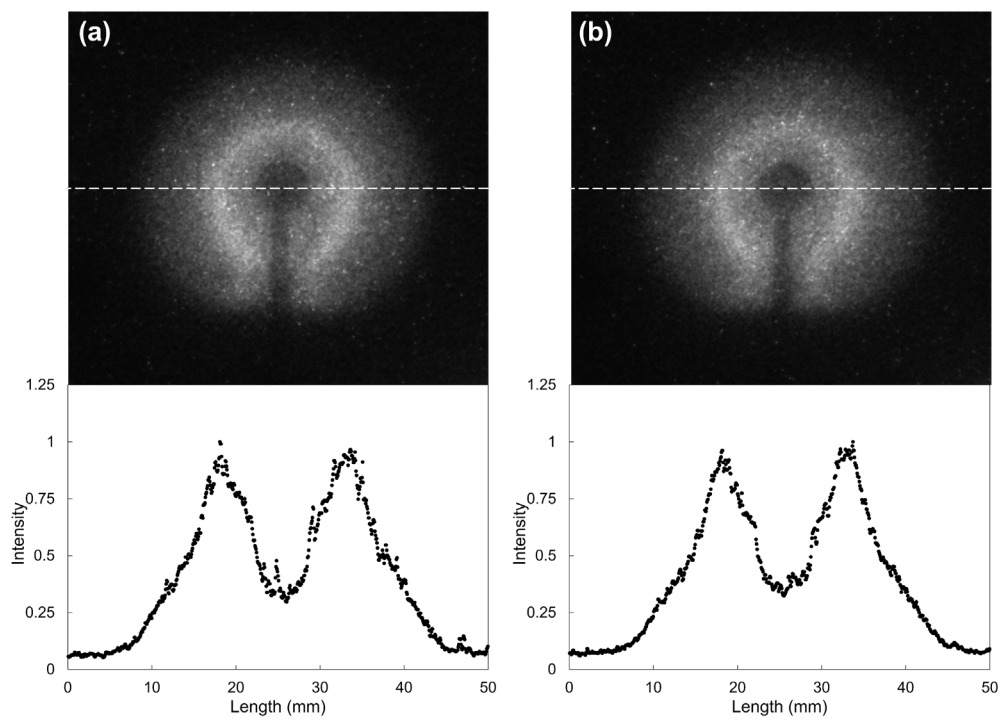


Fig. D.3. Averaged image of the cool flame and a plot of the pixel values along the dashed line: (a) Test D and (b) Test E.

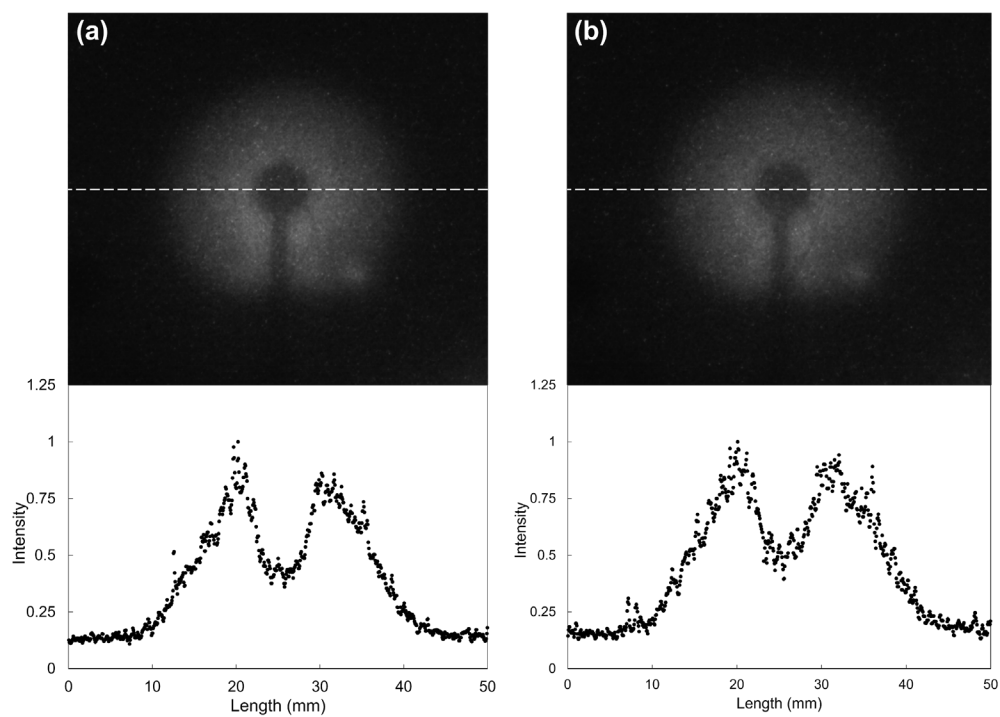


Fig. D.5. Averaged image of the cool flame and a plot of the pixel values along the dashed line: (a) Test F1 and (b) Test F2.

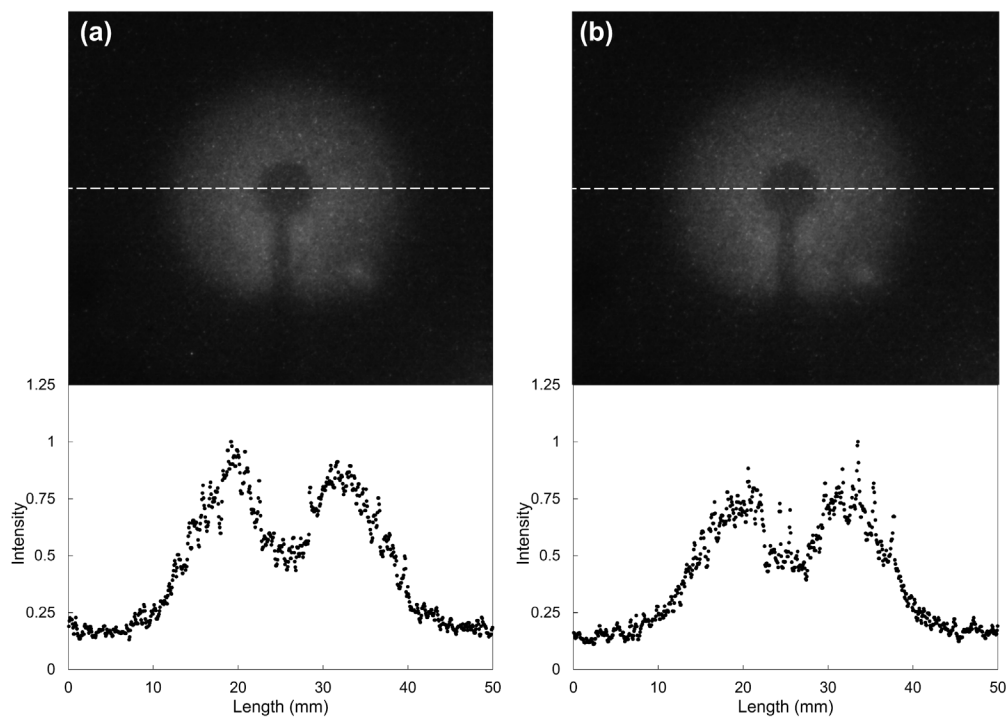


Fig. D.7. Averaged image of the cool flame and a plot of the pixel values along the dashed line: (a) Test F3 and (b) Test F4.

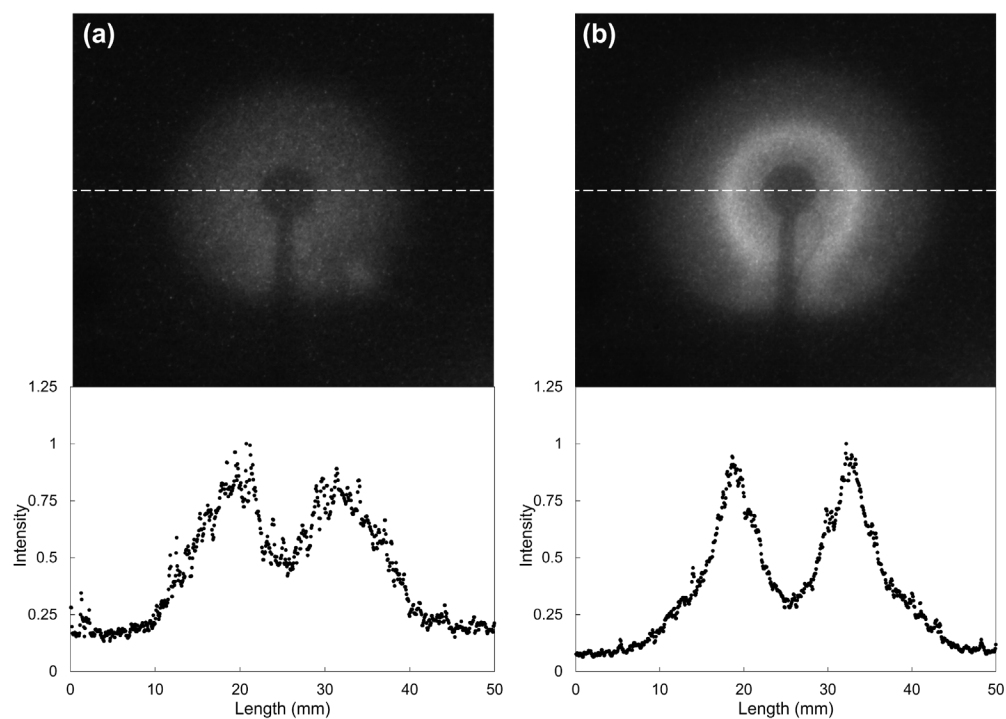


Fig. D.9. Averaged image of the cool flame and a plot of the pixel values along the dashed line: (a) Test F5 and (b) Test G1.

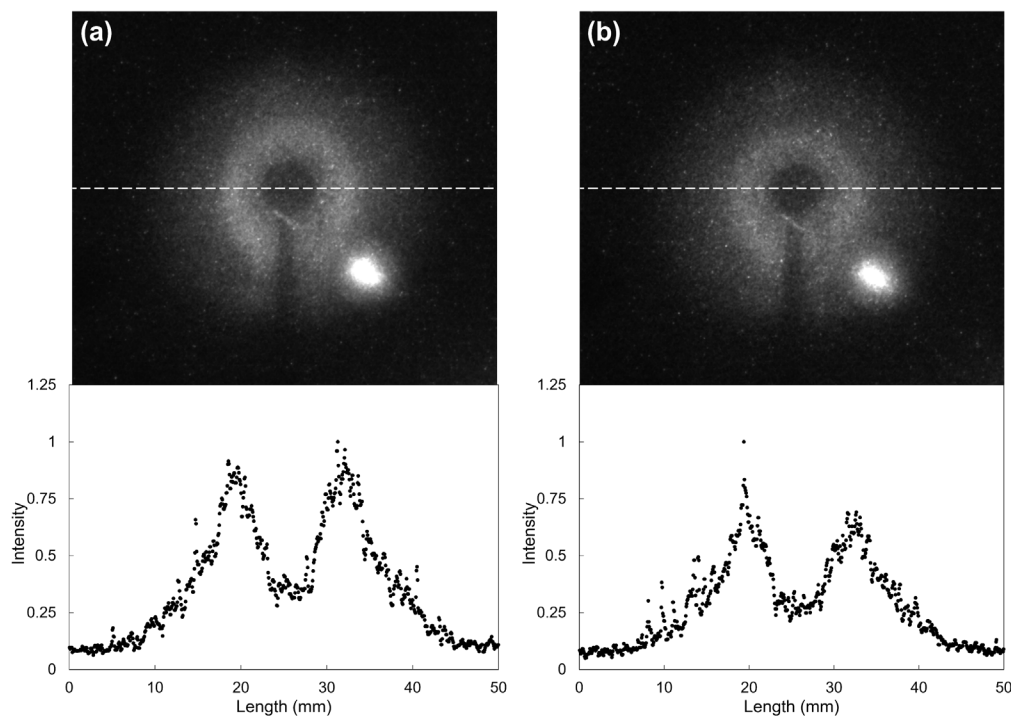


Fig. D.11. Averaged image of the cool flame and a plot of the pixel values along the dashed line: (a) Test G2 and (b) Test G3.

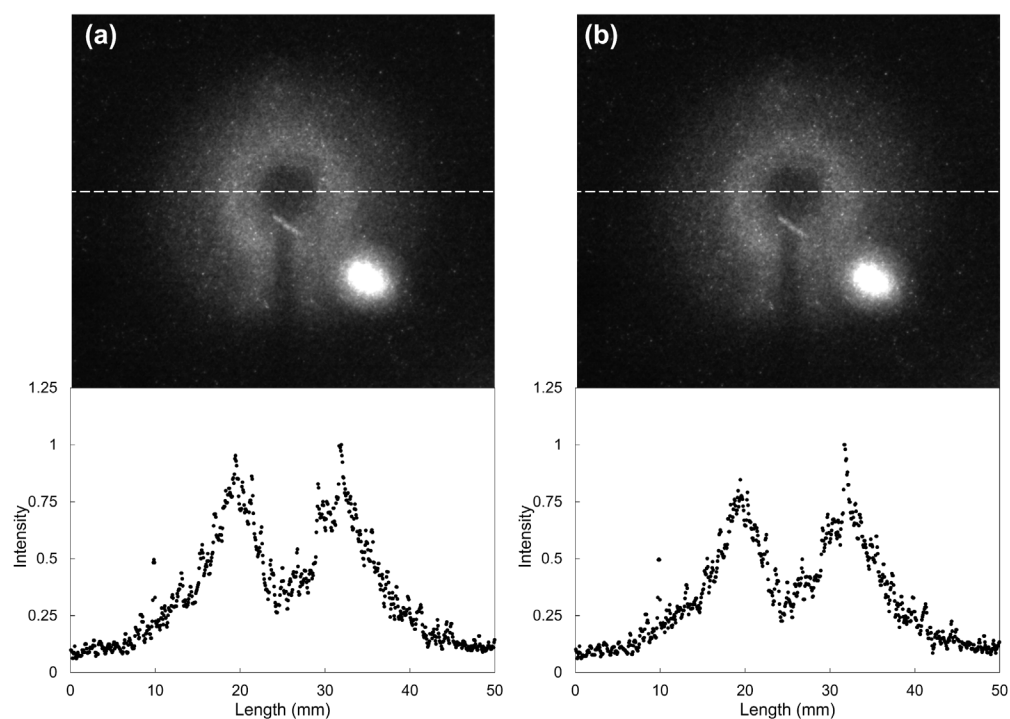


Fig. D.13. Averaged image of the cool flame and a plot of the pixel values along the dashed line: (a) Test G4 and (b) Test G5.

Appendix E. CFI-G Test Matrices

The first five digits of the test point number mean year and day-of-year (e.g., 21001 denotes Jan 1, 2021). in Test point numbers corresponding to the test identifications used in Table 4.2 are shown in Table E.1. The summary of CFI-G test matrices for normal flames and inverse flames is shown along in Tables E.2 to E.9 below.

Table E.1. Corresponding test point numbers to the test IDs in Table 4.2

Test ID in Table 4.2	Test point in Appendix D
A	21174C6
B	21174C4
C	21174D1
D	21174C3
E	21174F1
F1-5	21291C1
G1-5	21291A1

Table E.2. CFI-G test matrix for test day 21088, 21102, and 21106 (normal flames)

Test point	Fuel	X_{O_2} before test	X_{O_2} after test	p (atm)	X_{HC}	\dot{m}_{HC} (mg/s)	TFP ^a	T_{ad} (K)	Z_{st}	Hot ignition	Hot flame duration (s)	Type of extinction (RE or FT)	Peak burner temperature (K)
21088A1	ethane	0.39	0.39	0.9	1.00	2.00	No	2719	0.103	Yes	50	SE	564
21088B1	ethane	0.39	0.39	0.9	1.00	2.00	Yes	2714	0.102	Yes	43	SE	549
21088C1	ethane	0.39	0.38	0.9	1.00	2.00	Yes	2709	0.101	Yes	42	SE	540
21088D1	ethane	0.38	0.38	0.9	1.00	1.00	Yes	2704	0.100	Yes	61	FT	732
21088F1	ethane	0.38	0.38	0.9	1.00	0.50	Yes	2700	0.100	Yes	28	FT	805
21088G1	ethane	0.38	0.38	0.9	0.50	2.00	No	2639	0.176	Yes	42	SE	500
21088H1	ethane	0.38	0.37	0.9	0.50	1.00	Yes	2634	0.175	Yes	62	FT	690
21088J1	ethane	0.37	0.37	0.9	0.25	2.00	Yes	2512	0.292	Yes	37	SE	437
21088K1	ethane	0.37	0.36	0.9	0.25	1.00	Yes	2507	0.290	Yes	98	FT	613
21088H2	ethane	0.36	0.36	0.9	0.50	1.00	Yes	2616	0.170	Yes	127	FT	695
21088M4	ethane	0.21	0.21	1.0	1.00	1.00	Yes	2257	0.059	Yes	13	SE	398
21088L1	ethane	0.21	0.21	1.0	1.00	2.00	No	2254	0.059	Yes	9	SE	354
21088N1	ethane	0.18	0.18	1.0	0.50	2.00	Yes	2043	0.094	Yes	7	SE	326
21088P1	ethane	0.18	0.18	1.0	0.50	1.00	Yes	2040	0.094	Yes	8	SE	347
21102A1	butane	0.40	0.39	1.0	0.25	1.60	No	2633	0.226	Yes	40	SE	504
21102C1	butane	0.39	0.39	1.0	0.50	1.60	No	2694	0.150	Yes	41	SE	542
21102B1	butane	0.39	0.39	1.0	0.13	1.30	No	2501	0.341	Yes	38	SE	469
21102C2	butane	0.39	0.39	1.0	0.50	0.80	No	2687	0.148	Yes	63	FT	778
21102C3	butane	0.39	0.38	1.0	0.50	1.20	No	2684	0.148	Yes	82	SE	661
21102C4	butane	0.38	0.38	1.0	0.50	0.80	No	2679	0.146	No	0	-	-
21102C5	butane	0.38	0.38	1.0	0.50	0.80	No	2679	0.146	Yes	43	FT	722
21102C6	butane	0.38	0.38	1.0	0.50	0.80	No	2677	0.146	No	0	-	-
21102C7	butane	0.38	0.38	1.0	0.50	0.80	No	2677	0.146	Yes	18	FT	571
21102C8	butane	0.38	0.38	1.0	0.50	0.80	No	2676	0.146	No	0	-	-
21102M1	butane	0.23	0.23	1.0	0.50	1.60	No	2337	0.097	Yes	8	SE	348
21102M2	butane	0.23	0.23	1.0	0.50	0.80	No	2335	0.097	Yes	14	SE	412
21102M3	butane	0.23	0.23	1.0	0.50	0.80	No	2334	0.096	No	0	-	-
21102M4	butane	0.23	0.23	1.0	0.50	0.80	No	2334	0.096	No	0	-	-
21102M5	butane	0.23	0.23	1.0	0.50	0.80	No	2334	0.096	No	0	-	-
21102M6	butane	0.23	0.23	1.0	0.50	0.80	No	2334	0.096	No	0	-	-
21106A4	butane	0.39	0.38	0.5	0.25	1.60	No	2629	0.225	Yes	60	SE	556
21106B1	butane	0.38	0.38	0.5	0.50	1.60	No	2682	0.147	Yes	62	SE	589
21106C1	butane	0.38	0.37	0.5	0.13	1.30	No	2482	0.333	Yes	63	SE	515
21106D1	butane	0.37	0.36	0.5	0.50	1.20	No	2659	0.142	Yes	120	SE	677
21106F1	butane	0.36	0.35	0.5	0.50	0.80	No	2642	0.139	Yes	72	FT	778
21106F2	butane	0.35	0.35	0.5	0.50	0.80	No	2635	0.138	No	0	-	-
21106F3	butane	0.35	0.35	0.5	0.50	0.50	No	2635	0.138	Yes	13	FT	586
21106F4	butane	0.35	0.35	0.5	0.50	0.50	No	2635	0.137	No	22	FT	675
21106F5	butane	0.35	0.35	0.5	0.50	0.50	No	2633	0.137	No	0	-	-
21106G6	butane	0.21	0.21	0.5	0.50	0.80	No	2233	0.088	Yes	20	SE	468
21106G7	butane	0.21	0.21	0.5	0.50	0.80	No	2228	0.087	Yes	20	SE	477
21106G9	butane	0.21	0.21	0.5	0.50	0.80	No	2223	0.087	Yes	14	SE	402
21106H1	butane	0.21	0.21	0.5	0.50	0.80	No	2219	0.087	No	0	-	-
21106H2	butane	0.21	0.21	0.5	0.50	0.80	No	2219	0.087	No	0	-	-

^a Thin filament pyrometry

Table E.3. CFI-G test matrix for test day 21112 and 21125 (normal flames)

Test point	Fuel	X_{O_2} before test	X_{O_2} after test	p (atm)	X_{HC}	\dot{m}_{HC} (mg/s)	TFP	T_{ad} (K)	Z_{st}	Hot ignition	Hot flame duration (s)	Type of extinction (RE or FT)	Peak burner temperature (K)
21112A1	propane	0.40	0.39	0.9	1.00	0.80	No	2730	0.105	Yes	43	FT	786
21112A2	propane	0.39	0.39	0.9	1.00	1.60	No	2728	0.105	Yes	44	SE	580
21112A3	propane	0.39	0.39	0.9	1.00	1.20	No	2724	0.105	Yes	95	SE	696
21112A4	propane	0.39	0.38	0.9	1.00	1.00	No	2718	0.103	Yes	185	FT	745
21112A5	propane	0.38	0.38	0.9	1.00	2.00	No	2707	0.102	Yes	24	SE	474
21112C1	propane	0.38	0.38	0.9	1.00	0.50	No	2704	0.101	Yes	29	FT	802
21112C2	propane	0.38	0.38	0.9	1.00	0.50	No	2703	0.101	Yes	29	FT	803
21112A6	propane	0.38	0.37	0.9	1.00	1.00	No	2702	0.101	Yes	259	SE	734
21112C3	propane	0.37	0.37	0.9	1.00	0.50	No	2687	0.099	No	0	-	-
21112C4	propane	0.37	0.37	0.9	1.00	0.50	No	2687	0.099	No	0	-	-
21112C5	propane	0.37	0.37	0.9	1.00	0.50	No	2687	0.099	No	0	-	-
21112C6	propane	0.37	0.37	0.9	1.00	0.50	No	2687	0.099	No	0	-	-
21112F1	propane	0.21	0.21	1.0	1.00	1.00	No	2276	0.061	No	0	-	-
21112F2	propane	0.21	0.21	1.0	1.00	1.00	No	2276	0.061	Yes	8	SE	368
21112F3	propane	0.21	0.21	1.0	1.00	0.80	No	2274	0.061	Yes	8	SE	378
21112F4	propane	0.21	0.21	1.0	1.00	0.60	No	2273	0.061	Yes	10	SE	410
21112F5	propane	0.21	0.21	1.0	1.00	0.40	No	2272	0.061	No	0	-	-
21112H1	propane	0.21	0.21	1.0	1.00	0.50	No	2272	0.061	Yes	12	SE	427
21112H2	propane	0.21	0.21	1.0	1.00	0.50	No	2271	0.061	Yes	11	SE	429
21112H3	propane	0.21	0.21	1.0	1.00	0.50	No	2271	0.061	No	0	-	-
21125A1	butane	0.39	0.39	1.0	0.02	0.50	No	1596	0.712	No	0	-	-
21125A2	butane	0.39	0.39	1.0	0.03	0.50	No	1795	0.657	Yes	8	SE	333
21125A3	butane	0.39	0.39	1.0	0.03	0.50	No	1695	0.685	No	0	-	-
21125A4	butane	0.39	0.39	1.0	0.00	0.00	No	-	-	No	0	-	-
21125A5	butane	0.39	0.39	1.0	0.03	0.50	No	1695	0.685	No	0	-	-
21125A6	butane	0.39	0.39	1.0	0.03	0.75	No	1695	0.685	No	0	-	-
21125A7	butane	0.39	0.39	1.0	0.03	0.25	No	1695	0.685	No	0	-	-
21125A8	butane	0.39	0.39	1.0	0.03	1.50	No	1695	0.685	No	0	-	-
21125A9	butane	0.39	0.39	1.0	0.03	2.36	No	1695	0.685	No	0	-	-
21125H1	butane	0.39	0.39	1.0	0.03	0.50	No	1695	0.685	No	0	-	-
21125H2	butane	0.39	0.39	1.0	0.03	0.50	No	1695	0.685	No	0	-	-
21125H3	butane	0.39	0.39	1.0	0.00	0.00	No	-	-	No	0	-	-
21125H4	butane	0.39	0.39	1.0	0.03	0.50	No	1695	0.685	No	0	-	-
21125J1	butane	0.39	0.39	1.0	0.02	0.50	No	1397	0.762	No	0	-	-
21125H5	butane	0.39	0.39	1.0	0.03	0.10	No	1695	0.685	No	0	-	-
21125K1	butane	0.39	0.39	1.0	0.03	1.50	No	1795	0.657	Yes	35	SE	500
21125K2	butane	0.39	0.38	1.0	0.03	3.00	No	1790	0.654	Yes	17	SE	389
21125K3	butane	0.38	0.38	1.0	0.03	0.75	No	1785	0.651	Yes	125	FT	754
21125D1	butane	0.21	0.21	1.0	0.05	0.50	No	1701	0.423	Yes	1	SE	307
21125D2	butane	0.21	0.21	1.0	0.05	0.50	No	1701	0.423	Yes	1	SE	305
21125D3	butane	0.21	0.21	1.0	0.05	0.50	No	1701	0.423	No	0	-	-
21125D4	butane	0.21	0.21	1.0	0.05	1.00	No	1701	0.423	No	0	-	-
21125D5	butane	0.21	0.21	1.0	0.05	2.00	No	1701	0.423	No	0	-	-
21125D6	butane	0.21	0.21	1.0	0.05	0.25	No	1701	0.423	No	0	-	-

Table E.4. CFI-G test matrix for test day 21130, 21137, and 21153 (normal flames)

Test point	Fuel	X_{O_2} before test	X_{O_2} after test	p (atm)	X_{HC}	\dot{m}_{HC} (mg/s)	TFP	T_{ad} (K)	Z_{st}	Hot ignition	Hot flame duration (s)	Type of extinction (RE or FT)	Peak burner temperature (K)
21130A1	propane	0.21	0.21	2.0	0.05	0.50	No	1602	0.470	Yes	1	SE	313
21130A2	propane	0.21	0.21	2.0	0.05	1.00	No	1602	0.470	Yes	1	SE	307
21130A3	propane	0.21	0.21	2.0	0.05	1.00	No	1602	0.470	No	0	-	-
21130A4	propane	0.21	0.21	2.0	0.05	1.00	No	1602	0.470	No	0	-	-
21130A5	propane	0.21	0.21	2.0	0.05	1.00	No	1602	0.470	Yes	1	SE	307
21130A6	propane	0.21	0.21	2.0	0.05	2.00	No	1602	0.470	No	0	-	-
21130A7	propane	0.21	0.21	2.0	0.05	2.50	No	1602	0.470	No	0	-	-
21130A8	propane	0.21	0.21	2.0	0.05	2.89	No	1602	0.470	No	0	-	-
21130A9	propane	0.21	0.21	2.0	0.05	0.25	No	1602	0.470	Yes	1	SE	411
21130M1	propane	0.21	0.21	2.0	0.30	1.00	No	2171	0.138	Yes	6	SE	338
21130M2	propane	0.21	0.21	2.0	0.30	2.00	No	2170	0.138	Yes	7	SE	330
21130M3	propane	0.21	0.21	2.0	0.30	0.50	No	2169	0.138	Yes	5	SE	343
21130G1	propane	0.22	0.22	3.0	0.05	0.50	No	1618	0.477	No	0	-	-
21130G2	propane	0.22	0.22	3.0	0.05	0.50	No	1618	0.477	Yes	1	SE	309
21130G3	propane	0.22	0.22	3.0	0.05	1.00	No	1618	0.477	Yes	1	SE	306
21130G4	propane	0.22	0.22	3.0	0.05	2.00	No	1618	0.477	No	0	-	-
21130G5	propane	0.22	0.22	3.0	0.05	2.89	No	1618	0.477	No	0	-	-
21130G6	propane	0.22	0.22	3.0	0.05	0.25	No	1618	0.477	Yes	1	SE	307
21130G7	propane	0.22	0.22	3.0	0.05	0.13	No	1618	0.477	Yes	1	SE	310
21130N1	propane	0.22	0.22	3.0	0.30	1.00	No	2198	0.141	Yes	6	SE	346
21130N2	propane	0.22	0.22	3.0	0.30	2.00	No	2198	0.141	Yes	6	SE	330
21130N3	propane	0.22	0.22	3.0	0.30	0.50	No	2197	0.141	Yes	5	SE	363
21130N4	propane	0.22	0.22	3.0	0.30	0.50	No	2197	0.141	Yes	5	SE	363
21130N5	propane	0.22	0.22	3.0	0.30	0.25	No	2197	0.141	No	0	-	-
21137A1	propane	0.40	0.40	1.0	0.30	2.89	No	2637	0.228	Yes	19	SE	406
21137A2	propane	0.40	0.39	1.0	0.30	1.50	No	2634	0.227	Yes	39	SE	508
21137A3	propane	0.39	0.39	1.0	0.30	1.00	No	2630	0.226	Yes	124	SE	671
21137B1	propane	0.39	0.37	1.0	0.15	2.89	No	2486	0.348	Yes	127	FT	453
21137B2	propane	0.37	0.36	1.0	0.08	1.50	No	2216	0.480	Yes	147	FT	435
21137A4	propane	0.36	0.36	1.0	0.30	1.25	No	2576	0.210	Yes	35	SE	507
21137A5	propane	0.36	0.35	1.0	0.30	1.10	No	2573	0.209	Yes	44	SE	556
21137A6	propane	0.35	0.35	1.0	0.30	1.40	No	2570	0.208	Yes	22	SE	445
21137A7	propane	0.35	0.35	1.0	0.30	1.20	No	2568	0.208	Yes	33	SE	503
21137D1	propane	0.21	0.21	1.0	0.30	2.89	No	2168	0.137	Yes	8	SE	338
21137D2	propane	0.21	0.21	1.0	0.30	0.50	No	2164	0.137	Yes	11	SE	407
21137C1	propane	0.21	0.21	1.0	0.15	0.50	No	2034	0.227	Yes	8	SE	375
21153A1	ethane	0.39	0.38	0.5	0.30	2.36	No	2573	0.264	Yes	59	SE	472
21153A2	ethane	0.38	0.36	0.5	0.30	1.50	No	2555	0.258	Yes	88	SE	543
21153A3	ethane	0.36	0.34	0.5	0.30	1.00	No	2537	0.252	Yes	258	SE	647
21153F1	ethane	0.34	0.33	0.5	0.30	1.50	Yes	2499	0.240	Yes	44	SE	478
21153A4	ethane	0.33	0.33	0.5	0.30	0.50	No	2488	0.237	Yes	56	FT	782
21153A5	ethane	0.33	0.31	0.5	0.30	0.75	No	2483	0.236	Yes	274	FT	694
21153C1	ethane	0.40	0.40	2.0	0.30	2.36	No	2586	0.269	Yes	34	SE	446
21153C2	ethane	0.40	0.39	2.0	0.30	1.50	No	2584	0.268	Yes	51	SE	512
21153C3	ethane	0.39	0.39	2.0	0.30	1.00	No	2581	0.267	Yes	123	SE	631
21153G1	ethane	0.39	0.39	2.0	0.30	1.00	Yes	2578	0.265	Yes	131	SE	632
21153C4	ethane	0.39	0.38	2.0	0.30	0.75	No	2573	0.264	Yes	276	FT	709
21153C5	ethane	0.38	0.38	2.0	0.30	0.50	No	2567	0.262	Yes	49	FT	785
21153C6	ethane	0.38	0.38	2.0	0.30	1.50	No	2566	0.261	Yes	44	SE	496
21153C7	ethane	0.38	0.38	2.0	0.30	1.00	No	2564	0.261	Yes	61	FT	608

Table E.5. CFI-G test matrix for test day 21162, 21174, and 21291 (normal flames)

Test point	Fuel	X_{O_2} before test	X_{O_2} after test	p (atm)	X_{HC}	\dot{m}_{HC} (mg/s)	TFP	T_{ad} (K)	Z_{st}	Hot ignition	Hot flame duration (s)	Type of extinction (RE or FT)	Peak burner temperature (K)
21162A1	ethane	0.40	0.39	1.0	0.30	2.36	No	2588	0.269	Yes	43	SE	455
21162A2	ethane	0.39	0.39	1.0	0.30	1.50	No	2582	0.267	Yes	71	SE	535
21162A3	ethane	0.39	0.38	1.0	0.30	1.00	No	2575	0.265	Yes	232	SE	648
21162B1	ethane	0.38	0.37	1.0	0.30	1.00	Yes	2560	0.259	Yes	158	SE	634
21162A4	ethane	0.37	0.36	1.0	0.30	0.85	No	2550	0.256	Yes	304	SE	678
21162C1	ethane	0.21	0.21	1.0	0.30	0.50	No	2121	0.166	Yes	19	SE	435
21162C2	ethane	0.21	0.21	1.0	0.30	0.75	No	2119	0.165	Yes	11	SE	368
21162C3	ethane	0.21	0.21	1.0	0.30	1.00	No	2118	0.165	Yes	9	SE	346
21162C4	ethane	0.21	0.21	1.0	0.30	1.50	No	2116	0.165	Yes	9	SE	338
21162C5	ethane	0.21	0.21	1.0	0.30	2.36	No	2114	0.165	Yes	9	SE	336
21162D1	ethane	0.21	0.21	1.0	0.30	0.50	Yes	2110	0.164	Yes	16	SE	417
21162F1	ethane	0.21	0.21	1.0	0.30	1.50	No	2109	0.164	No	0	-	-
21162F2	ethane	0.21	0.21	1.0	0.30	1.50	No	2109	0.164	Yes	10	SE	340
21174A1	butane	0.39	0.38	0.5	0.30	3.22	No	2645	0.200	Yes	21	SE	405
21174A2	butane	0.38	0.38	0.5	0.30	2.00	No	2637	0.198	Yes	29	SE	448
21174A3	butane	0.38	0.37	0.5	0.30	1.50	No	2631	0.196	Yes	54	SE	549
21174A4	butane	0.37	0.36	0.5	0.30	1.00	No	2621	0.193	Yes	210	SE	694
21174B1	butane	0.36	0.35	0.5	0.30	1.00	Yes	2596	0.187	Yes	109	SE	661
21174C1	butane	0.40	0.40	2.0	0.30	3.22	No	2658	0.204	Yes	30	SE	429
21174C2	butane	0.40	0.40	2.0	0.30	2.00	No	2655	0.203	Yes	29	SE	463
21174C3	butane	0.40	0.39	2.0	0.30	1.50	No	2654	0.202	Yes	35	SE	519
21174C4	butane	0.39	0.39	2.0	0.30	1.00	No	2652	0.202	Yes	90	SE	672
21174D1	butane	0.39	0.39	2.0	0.30	1.00	Yes	2650	0.201	Yes	83	SE	666
21174F1	butane	0.39	0.39	2.0	0.30	1.50	No	2648	0.201	Yes	40	SE	531
21174C5	butane	0.39	0.39	2.0	0.30	0.50	No	2646	0.200	Yes	34	FT	791
21174C6	butane	0.39	0.39	2.0	0.30	0.75	No	2646	0.200	Yes	251	SE	761
21174F2	butane	0.39	0.38	2.0	0.30	1.50	No	2640	0.199	Yes	24	FT	473
21174F3	butane	0.38	0.38	2.0	0.30	1.50	No	2639	0.198	Yes	23	FT	476
21174F4	butane	0.38	0.38	2.0	0.30	1.50	No	2638	0.198	Yes	35	FT	515
21291A1	butane	0.40	0.39	2.0	0.30	1.50	No	2659	0.204	Yes	167	FT	637
21291C1	butane	0.39	0.39	2.0	0.30	1.00	No	2652	0.202	Yes	246	FT	708
21291C2	butane	0.39	0.39	2.0	0.30	1.75	No	2646	0.200	Yes	27	SE	455
21291B1	butane	0.39	0.39	2.0	0.30	1.75	Yes	2644	0.200	Yes	32	SE	466
21291H1	butane	0.39	0.39	2.0	0.15	1.25	No	2538	0.304	Yes	35	SE	489
21291H2	butane	0.39	0.38	2.0	0.15	0.75	No	2537	0.304	Yes	158	FT	729
21291D1	butane	0.40	0.39	1.0	0.30	1.50	No	2657	0.203	Yes	47	SE	531
21291G1	butane	0.39	0.39	1.0	0.30	1.00	No	2653	0.202	Yes	161	SE	701
21291G2	butane	0.39	0.39	1.0	0.30	1.25	No	2644	0.200	Yes	60	SE	584
21291J1	butane	0.39	0.38	1.0	0.15	0.75	No	2536	0.303	Yes	80	FT	727
21291J2	butane	0.38	0.38	1.0	0.15	1.50	No	2532	0.302	Yes	27	SE	425
21291J3	butane	0.38	0.38	1.0	0.15	1.00	No	2530	0.301	Yes	83	SE	603

Table E.6. CFI-G test matrix for test day 21196, 21202, and 21209 (inverse flames)

Test point	Fuel	X_{HC} before test	X_{HC} after test	P (atm)	X_{O_2}	\dot{m}_{O_2} (mg/s)	TFP	T_{ad} (K)	Z_{st}	Hot ignition	Hot flame duration (s)	Type of extinction (RE or FT)	Peak burner temperature (K)
21196A1	ethane	0.30	0.30	1.0	0.21	5.59	No	2120	0.166	No	0	-	300
21196A2	ethane	0.30	0.30	1.0	0.21	5.59	No	2120	0.166	Yes	35	FT	436
21196F1	ethane	0.30	0.29	1.0	0.15	5.59	No	1787	0.127	Yes	36	FT	392
21196H1	ethane	0.29	0.29	1.0	0.12	5.59	No	1567	0.106	No	0	-	300
21196J1	ethane	0.29	0.29	1.0	0.14	5.59	No	1680	0.117	Yes	1	SE	301
21196F2	ethane	0.29	0.29	1.0	0.15	2.79	No	1785	0.128	Yes	66	FT	442
21196F3	ethane	0.29	0.29	1.0	0.15	1.40	No	1783	0.130	Yes	1	SE	313
21196F4	ethane	0.29	0.29	1.0	0.15	2.10	No	1783	0.130	Yes	1	SE	339
21196F5	ethane	0.29	0.29	1.0	0.15	9.08	No	1783	0.130	Yes	1	SE	302
21196F6	ethane	0.29	0.28	1.0	0.15	2.79	No	1783	0.130	Yes	66	FT	440
21196K1	ethane	0.28	0.28	0.4	0.15	2.79	No	1781	0.131	Yes	1	SE	337
21196L1	ethane	0.28	0.28	0.4	0.21	2.79	No	2110	0.173	Yes	1	SE	396
21196L2	ethane	0.28	0.28	0.4	0.21	2.79	No	2110	0.173	Yes	63	FT	547
21196M1	ethane	0.28	0.28	0.4	0.30	2.79	No	2400	0.232	Yes	1	SE	410
21196M2	ethane	0.28	0.27	0.4	0.30	2.79	No	2400	0.232	Yes	66	FT	788
21196M2_1	ethane	0.27	0.26	0.4	0.30	5.59	No	2396	0.235	Yes	64	FT	788
21202A1	ethane	0.06	0.06	2.0	0.85	0.93	No	2078	0.784	No	0	-	300
21202A2	ethane	0.06	0.06	2.0	0.85	1.86	No	2078	0.784	Yes	2	SE	335
21202A3	ethane	0.06	0.06	2.0	0.85	3.72	No	2077	0.784	Yes	3.5	SE	324
21202A4	ethane	0.06	0.06	2.0	0.85	9.08	No	2077	0.784	Yes	5	SE	318
21202H1	ethane	0.12	0.12	2.0	0.85	3.72	No	2567	0.646	Yes	28	SE	487
21202H2	ethane	0.12	0.12	2.0	0.85	9.08	No	2566	0.646	Yes	16	SE	381
21202H3	ethane	0.12	0.12	2.0	0.85	1.86	No	2565	0.646	Yes	66	FT	742
21202H4	ethane	0.12	0.12	2.0	0.85	2.79	No	2564	0.647	Yes	41	SE	574
21202J1	ethane	0.12	0.12	2.0	0.85	2.79	Yes	2563	0.647	Yes	53	SE	601
21202K1	ethane	0.12	0.12	1.0	0.85	3.72	No	2561	0.648	Yes	55	SE	549
21202K2	ethane	0.12	0.12	1.0	0.85	9.08	No	2558	0.649	Yes	21	SE	387
21202L1	ethane	0.12	0.12	1.0	0.85	3.72	Yes	2555	0.651	Yes	50	SE	529
21209A1	ethane	0.24	0.24	0.5	0.85	3.72	No	2821	0.479	Yes	26	FT	817
21209A2	ethane	0.24	0.24	0.5	0.85	9.07	No	2820	0.480	No	0	-	299
21209A3	ethane	0.24	0.23	0.5	0.85	9.07	No	2820	0.480	Yes	67	FT	573
21209B1	ethane	0.23	0.22	0.5	0.85	9.07	Yes	2813	0.486	Yes	136	FT	573
21209A4	ethane	0.22	0.22	0.5	0.85	5.59	No	2797	0.500	Yes	66	FT	692
21209H1	ethane	0.22	0.21	0.5	0.50	5.59	No	2615	0.385	Yes	66	FT	563
21209J1	ethane	0.21	0.21	0.5	0.30	5.59	No	2332	0.283	Yes	66	FT	522
21209F1	ethane	0.21	0.20	0.5	0.21	5.59	No	2037	0.224	Yes	66	FT	475
21209F2	ethane	0.20	0.19	0.5	0.21	3.72	No	2026	0.231	Yes	66	FT	487
21209F3	ethane	0.19	0.19	0.5	0.21	1.86	No	2019	0.235	Yes	66	FT	590
21209B2	ethane	0.19	0.19	0.5	0.85	3.72	Yes	2750	0.537	Yes	48	FT	787
21209K1	ethane	0.19	0.19	0.5	0.18	1.86	No	1874	0.213	Yes	26	FT	401

Table E.7. CFI-G test matrix for test day 21216, 21222, 21228, and 21235 (inverse flames)

Test point	Fuel	X_{HC} before test	X_{HC} after test	P (atm)	X_{O_2}	\dot{m}_{O_2} (mg/s)	TFP	T_{ad} (K)	Z_{st}	Hot ignition	Hot flame duration (s)	Type of extinction (RE or FT)	Peak burner temperature (K)
21216A1	ethane	0.10	0.10	3.0	0.85	3.72	No	2468	0.686	Yes	17	SE	433
21216A2	ethane	0.10	0.10	3.0	0.85	5.59	No	2468	0.686	Yes	15	SE	392
21216A3	ethane	0.10	0.10	3.0	0.85	9.07	No	2467	0.686	Yes	15	SE	373
21216A4	ethane	0.10	0.10	3.0	0.85	1.86	No	2466	0.687	Yes	36	SE	604
21216A5	ethane	0.10	0.10	3.0	0.85	0.93	No	2466	0.687	Yes	1	SE	333
21216A6	ethane	0.10	0.10	3.0	0.85	1.40	No	2466	0.687	Yes	66	FT	745
21216B1	ethane	0.10	0.10	3.0	0.85	5.59	Yes	2465	0.687	Yes	25	SE	416
21216C1	ethane	0.10	0.10	3.0	0.50	5.59	No	2292	0.575	Yes	12	SE	351
21216F1	ethane	0.10	0.10	3.0	0.21	5.59	No	1786	0.372	Yes	68	FT	400
21216H1	ethane	0.10	0.10	1.0	0.85	5.59	No	2458	0.689	Yes	20	SE	394
21216H2	ethane	0.10	0.10	1.0	0.85	9.07	No	2456	0.690	Yes	18	SE	372
21216J1	ethane	0.10	0.10	1.0	0.50	3.72	No	2280	0.580	Yes	19	SE	384
21216K1	ethane	0.10	0.10	1.0	0.21	3.72	No	1776	0.377	Yes	66	FT	405
21222A1	propane	0.08	0.08	3.0	0.85	5.44	No	2533	0.665	Yes	10	SE	375
21222A2	propane	0.08	0.08	3.0	0.85	3.63	No	2532	0.665	Yes	16	SE	422
21222A3	propane	0.08	0.08	3.0	0.85	9.07	No	2532	0.665	Yes	18	SE	374
21222A4	propane	0.08	0.08	3.0	0.85	1.81	No	2531	0.665	Yes	13	SE	451
21222A5	propane	0.08	0.08	3.0	0.85	1.36	No	2531	0.665	Yes	3	SE	366
21222B1	propane	0.08	0.08	3.0	0.85	5.44	Yes	2531	0.665	Yes	17	SE	392
21222C1	propane	0.08	0.08	3.0	0.50	5.44	No	2359	0.551	Yes	6	SE	328
21222C2	propane	0.08	0.08	3.0	0.50	3.63	No	2358	0.551	Yes	8	SE	341
21222F1	propane	0.08	0.08	3.0	0.21	5.44	No	1834	0.349	Yes	1	SE	299
21222F2	propane	0.08	0.08	3.0	0.21	1.81	No	1834	0.349	No	0	-	300
21228A1	propane	0.09	0.09	2.0	0.85	5.44	No	2587	0.640	Yes	8	SE	362
21228A2	propane	0.09	0.09	2.0	0.85	9.07	No	2587	0.641	Yes	11	SE	355
21228A3	propane	0.09	0.09	2.0	0.85	3.63	No	2586	0.641	Yes	12	SE	400
21228A4	propane	0.09	0.09	2.0	0.85	1.81	No	2586	0.641	Yes	12	SE	443
21228B1	propane	0.09	0.09	2.0	0.85	5.44	Yes	2585	0.641	Yes	16	SE	385
21228C1	propane	0.09	0.09	2.0	0.50	5.44	No	2414	0.524	Yes	8	SE	336
21228C2	propane	0.09	0.09	2.0	0.50	9.07	No	2414	0.524	Yes	66	FT	420
21228C3	propane	0.09	0.09	2.0	0.50	3.63	No	2409	0.527	Yes	7	SE	335
21228C4	propane	0.09	0.09	2.0	0.50	1.81	No	2408	0.527	Yes	9	SE	415
21228F1	propane	0.09	0.09	2.0	0.21	5.44	No	1873	0.328	Yes	65	FT	391
21228H1	propane	0.09	0.09	1.0	0.85	5.44	No	2573	0.647	Yes	8	SE	351
21228H2	propane	0.09	0.09	1.0	0.85	1.81	No	2573	0.647	Yes	15	SE	456
21228J1	propane	0.09	0.09	1.0	0.85	1.81	Yes	2572	0.647	Yes	18	SE	472
21228K1	propane	0.09	0.09	1.0	0.50	5.44	No	2401	0.531	Yes	9	SE	340
21228K2	propane	0.09	0.09	1.0	0.50	1.81	No	2400	0.531	Yes	12	SE	439
21228L1	propane	0.09	0.09	1.0	0.21	3.63	No	1866	0.331	Yes	3	SE	303
21228L2	propane	0.09	0.09	1.0	0.21	5.44	No	1866	0.331	Yes	16	FT	341
21235A1	propane	0.21	0.20	1.0	0.85	5.44	No	2861	0.452	Yes	66	FT	637
21235A2	propane	0.20	0.20	1.0	0.85	9.07	No	2860	0.453	Yes	66	FT	526
21235C1	propane	0.20	0.20	1.0	0.50	3.63	No	2674	0.340	Yes	66	FT	655
21235F1	propane	0.20	0.20	1.0	0.21	1.81	No	2103	0.185	Yes	66	FT	520
21235F2	propane	0.20	0.20	1.0	0.21	9.07	No	2101	0.186	No	0	-	299
21235H1	propane	0.20	0.20	1.0	0.18	1.36	No	1954	0.164	Yes	4	SE	328
21235J1	propane	0.20	0.20	1.0	0.19	1.81	No	2006	0.171	Yes	66	FT	454
21235B1	propane	0.20	0.19	1.0	0.85	5.44	Yes	2853	0.460	Yes	152	FT	685
21235K1	propane	0.19	0.19	0.5	0.85	5.44	No	2849	0.464	Yes	66	FT	674
21235L1	propane	0.19	0.18	0.5	0.85	9.07	Yes	2845	0.468	Yes	127	FT	564

Table E.8. CFI-G test matrix for test day 21242, 21256, 21265, and 21270 (inverse flames)

Test point	Fuel	X_{HC} before test	X_{HC} after test	p (atm)	X_{O_2}	\dot{m}_{O_2} (mg/s)	TFP	T_{ad} (K)	Z_{st}	Hot ignition	Hot flame duration (s)	Type of extinction (RE or FT)	Peak burner temperature (K)
21242A1	propane	0.43	0.43	0.5	0.85	5.44	No	2978	0.306	Yes	12	FT	925
21242P1	propane	0.43	0.42	0.5	0.30	5.44	No	2507	0.144	Yes	21	FT	447
21242F2	propane	0.42	0.42	0.5	0.21	5.44	No	2208	0.107	No	0	-	299
21242F3	propane	0.42	0.42	0.5	0.21	5.44	No	2208	0.107	No	0	-	299
21242F4	propane	0.42	0.42	0.5	0.21	3.63	No	2208	0.107	No	0	-	299
21242P2	propane	0.42	0.42	0.5	0.30	5.44	No	2506	0.144	No	0	-	299
21256A1	butane	0.09	0.09	2.0	0.85	5.37	No	2679	0.592	Yes	9	SE	375
21256A2	butane	0.09	0.09	2.0	0.85	3.58	No	2678	0.592	Yes	11	SE	404
21256A3	butane	0.09	0.09	2.0	0.85	1.79	No	2678	0.592	Yes	11	SE	448
21256A4	butane	0.09	0.09	2.0	0.85	1.34	No	2678	0.592	Yes	5	SE	400
21256A5	butane	0.09	0.09	2.0	0.85	8.95	No	2678	0.592	Yes	9	SE	357
21256C1	butane	0.09	0.09	2.0	0.50	5.37	No	2509	0.472	Yes	9	SE	337
21256F1	butane	0.09	0.09	2.0	0.21	5.37	No	1956	0.281	Yes	66	FT	405
21256B1	butane	0.09	0.09	2.0	0.85	5.37	Yes	2673	0.595	Yes	13	SE	385
21256C2	butane	0.09	0.09	2.0	0.50	1.79	No	2505	0.475	Yes	9	SE	428
21256H1	butane	0.07	0.07	2.0	0.85	5.37	No	2586	0.642	Yes	7	SE	352
21256H2	butane	0.07	0.07	2.0	0.85	3.58	No	2586	0.642	Yes	7	SE	362
21256H3	butane	0.07	0.07	2.0	0.85	1.79	No	2585	0.642	Yes	5	SE	374
21256H4	butane	0.07	0.07	2.0	0.85	1.34	No	2585	0.642	Yes	3	SE	349
21256H5	butane	0.07	0.07	2.0	0.85	8.95	No	2585	0.642	Yes	7	SE	342
21256K1	butane	0.07	0.07	2.0	0.50	5.37	No	2416	0.525	Yes	4	SE	316
21256M1	butane	0.07	0.07	2.0	0.21	5.37	No	1879	0.326	Yes	1	SE	299
21256J1	butane	0.07	0.07	2.0	0.85	5.37	Yes	2585	0.642	Yes	7	SE	349
21265A1	butane	0.06	0.06	3.0	0.85	5.37	No	2493	0.681	Yes	6	SE	349
21265A2	butane	0.06	0.06	3.0	0.85	3.58	No	2493	0.681	Yes	5	SE	355
21265A3	butane	0.06	0.06	3.0	0.85	1.79	No	2493	0.681	Yes	1	SE	347
21265A4	butane	0.06	0.06	3.0	0.85	2.68	No	2493	0.681	Yes	5	SE	364
21265A5	butane	0.06	0.06	3.0	0.85	8.95	No	2493	0.681	Yes	8	SE	342
21265C1	butane	0.06	0.06	3.0	0.50	5.37	No	2321	0.568	Yes	3	SE	312
21265C2	butane	0.06	0.06	3.0	0.50	8.95	No	2321	0.569	Yes	5	SE	319
21265C3	butane	0.06	0.06	3.0	0.50	3.58	No	2320	0.569	Yes	2	SE	312
21265F1	butane	0.06	0.06	3.0	0.21	5.37	No	1807	0.365	Yes	0.5	SE	299
21265F2	butane	0.06	0.06	3.0	0.21	8.95	No	1807	0.365	Yes	66	FT	398
21265F3	butane	0.06	0.06	3.0	0.21	3.58	No	1801	0.368	No	0	-	299
21265F4	butane	0.06	0.06	3.0	0.21	3.58	No	1801	0.368	No	0	-	299
21265H1	butane	0.06	0.06	3.0	0.40	5.37	No	2209	0.520	Yes	1	SE	307
21265H2	butane	0.06	0.06	3.0	0.40	8.95	No	2209	0.520	Yes	66	FT	408
21265J1	butane	0.06	0.06	3.0	0.70	8.95	No	2427	0.648	Yes	6	SE	330
21265K1	butane	0.06	0.06	3.0	0.45	8.95	No	2261	0.550	Yes	5	SE	317
21265H3	butane	0.06	0.06	3.0	0.40	8.95	No	2203	0.522	Yes	107	FT	273
21270A1	butane	0.17	0.17	1.0	0.85	5.37	No	2873	0.442	Yes	60	FT	602
21270A2	butane	0.17	0.17	1.0	0.85	8.95	No	2872	0.443	Yes	90	FT	514
21270A3	butane	0.17	0.17	1.0	0.85	2.68	No	2868	0.447	Yes	35	FT	733
21270A4	butane	0.17	0.17	1.0	0.85	4.03	No	2868	0.447	Yes	90	FT	706
21270C1	butane	0.17	0.17	1.0	0.50	5.37	No	2682	0.334	Yes	70	FT	484
21270H1	butane	0.14	0.14	1.0	0.85	5.37	No	2823	0.489	Yes	51	SE	517
21270H2	butane	0.14	0.14	1.0	0.85	2.68	No	2821	0.491	Yes	43	FT	728
21270H3	butane	0.14	0.14	1.0	0.85	4.03	No	2821	0.491	Yes	43	FT	626
21270H4	butane	0.14	0.14	1.0	0.85	8.95	No	2820	0.492	Yes	83	FT	490
21270H5	butane	0.14	0.14	1.0	0.85	4.69	No	2815	0.496	Yes	46	SE	534

Table E.9. CFI-G test matrix for test day 21277 (inverse flames)

Test point	Fuel	X_{HC} before test	X_{HC} after test	p (atm)	X_{O_2}	\dot{m}_{O_2} (mg/s)	TFP	T_{ad} (K)	Z_{st}	Hot ignition	Hot flame duration (s)	Type of extinction (RE or FT)	Peak burner temperature (K)
21277A1	butane	0.36	0.36	0.5	0.85	5.37	No	2978	0.309	Yes	12	FT	802
21277H1	butane	0.36	0.36	0.5	0.50	5.37	No	2788	0.216	Yes	17	FT	735
21277J1	butane	0.36	0.36	0.5	0.21	5.37	No	2210	0.108	No	0	-	299
21277K1	butane	0.36	0.36	0.5	0.30	5.37	No	2507	0.146	No	0	-	299
21277K2	butane	0.36	0.36	0.5	0.30	5.37	No	2507	0.146	Yes	20	FT	433
21277J2	butane	0.36	0.36	0.5	0.21	5.37	No	2209	0.108	No	0	-	299
21277C1	butane	0.25	0.25	0.5	0.85	5.37	No	2932	0.370	Yes	20	FT	678
21277C2	butane	0.25	0.25	0.5	0.85	8.95	No	2932	0.371	Yes	36	FT	562
21277L1	butane	0.25	0.24	0.5	0.50	5.37	No	2744	0.268	Yes	66	FT	660
21277F1	butane	0.18	0.18	0.5	0.85	5.37	No	2878	0.436	Yes	66	FT	666
21277F2	butane	0.18	0.17	0.5	0.85	8.95	No	2876	0.439	Yes	66	FT	715
21277M1	butane	0.14	0.14	0.5	0.85	8.95	No	2824	0.489	Yes	66	FT	729
21277N1	butane	0.14	0.14	0.5	0.50	2.98	No	2643	0.370	Yes	55	FT	731
21277P1	butane	0.14	0.14	0.5	0.30	1.83	No	2369	0.266	Yes	40	FT	731

Appendix F. CFI-G Test Parameters

Table F.1. CFI-G test parameters for cool flame conditions (part 1)

testpointName	21174C3	21174C4	21174D1	21174F1	21174C6	21291A1	21291C1
dataCameraPreIgnitionExposureUs	1000000	1000000	1000000	1000000	1000000	1000000	1000000
dataCameraTestExposureUs	100000	100000	100000	100000	100000	1000000	5000000
analogCameraShutter	2	2	2	2	2	2	2
useIntensifiedCamera	TRUE	TRUE	TRUE	TRUE	TRUE	TRUE	TRUE
intensifierIgnitionGain	20000	20000	20000	20000	20000	20000	20000
intensifierTestGain	60000	60000	60000	60000	60000	80000	80000
preIgnitionImageTimeSec	0	0	0	0	0	0	0
postFlameImagingTimeSec	5	5	5	5	5	5	5
useDataCameraAutoGain	FALSE	FALSE	FALSE	FALSE	FALSE	FALSE	FALSE
autoGainTolerancePercent	5	5	5	5	5	5	5
autoGainMaxDb	33	33	33	33	33	33	33
autoGainMinDb	0	0	0	0	0	0	0
autoGainOutliers	0	0	0	0	0	0	0
autoGainRatePercent	100	100	100	100	100	100	100
autoGainTargetPercent	50	50	50	50	50	50	50
rampDataCameraGain	FALSE	FALSE	FALSE	FALSE	FALSE	FALSE	FALSE
dataCameraGain1dB	0	0	0	0	0	0	0
dataCameraGain2dB	0	0	0	0	0	0	0
dataCameraGain3dB	0	0	0	0	0	0	0
dataCameraHoldTime1Sec	0	0	0	0	0	0	0
dataCameraHoldTime2Sec	0	0	0	0	0	0	0
dataCameraRamp1to2TimeSec	5	5	5	5	5	5	5
dataCameraRamp2to3TimeSec	5	5	5	5	5	5	5
dataCameraManualGain	33	33	0	33	33	33	33
useBracketedExposures	FALSE	FALSE	TRUE	FALSE	FALSE	FALSE	FALSE
bracketingImagesPerExposure	1	1	1	1	1	1	1
bracketingNumberOfExposures	4	4	4	4	4	4	4
bracketingExposureStartUseC	5000	5000	50000	5000	5000	500000	500000
bracketingExposureMultiplierTimes100	1000	1000	200	1000	1000	160	160
igniterStartPosition	2170	2170	2170	2170	2170	2170	2170
igniterEndPosition	2290	2290	2290	2290	2290	2290	2290
igniterVelocityCountsPerSec	80	80	80	80	80	80	80
igniterPreheatPowerV	3	3	3	2.8	3	3	3
igniterPreheatDurationMs	1000	1000	1000	10000	1000	1000	1000
igniterIgnitionPowerV	4	4	4	3	4	4	4
igniterIgnitionDurationMs	3000	3000	3000	10000	3000	3000	3000
igniterDelayBeforeRetractMs	1800	1800	1800	8200	1800	1800	1800
igniterRetractVelocityCountsPerSec	500	500	500	500	500	500	500
pmt1Gain	5.5	5.5	5.5	5.5	6	6	6
pmt2Gain	6.0	6.0	6.0	6.0	6.5	6.5	6.5
pmt3Gain	6.0	6.0	5.5	6.0	6.5	6.5	6.5
fiberIgnitionPosition	0	0	10000	0	0	0	0
fiberTestPosition	0	0	17000	0	0	0	0
fiberMoveDuringTest	FALSE	FALSE	FALSE	FALSE	FALSE	FALSE	FALSE
fiberSegmentDistance	100	100	100	100	100	100	100
fiberVelocity	3000	3000	3000	3000	3000	3000	3000
fiberHoldDurationSec	1	1	1	1	1	1	1
fiberCycles	100	100	100	100	100	100	100

Table F.2. CFI-G test parameters for cool flame conditions (part 2)

testpointName	21174C3	21174C4	21174D1	21174F1	21174C6	21291A1	21291C1
useFoma	TRUE	TRUE	TRUE	TRUE	TRUE	TRUE	TRUE
flowTimeoutSec	360	360	360	360	360	270	270
fuelFlowIgnitionDeltaMs	0	0	0	0	0	2000	0
nitrogenFlowIgnitionDeltaMs	0	0	0	0	0	0	0
stabilizationTime1Sec	0	0	0	0	0	0	0
stabilizationTime2Sec	5	5	5	5	5	5	5
fuelIgnitionFlowSlpm	0.233	0.155	0.155	0.233	0.116	0.233	0.155
nitrogenIgnitionFlowSlpm	0.000	0.000	0.000	0.000	0.000	0.000	0.000
fuelTestFlow1Slpm	0.233	0.155	0.155	0.233	0.116	0.233	0.155
nitrogenTestFlow1Slpm	0.000	0.000	0.000	0.000	0.000	0.000	0.000
fuelTestFlow2Slpm	0.000	0.000	0.000	0.000	0.000	0.000	0.000
nitrogenTestFlow2Slpm	0.000	0.000	0.000	0.000	0.000	0.000	0.000
fuelTestFlow3Slpm	0.000	0.000	0.000	0.000	0.000	0.000	0.000
nitrogenTestFlow3Slpm	0.000	0.000	0.000	0.000	0.000	0.000	0.000
constantFlowTime1Sec	330	330	330	330	330	240	240
constantFlowTime2Sec	0	0	0	0	0	0	0
constantFlowTime3Sec	0	0	0	0	0	0	0
ignitionToTestRampTimeSec	0	0	0	0	0	0	0
testFlowRamp1To2TimeSec	0	0	0	0	0	0	0
testFlowRamp2To3TimeSec	0	0	0	0	0	0	0
postExtinctionDelaySec	3	3	3	3	3	3	3
postExtinctionFlowChangeFuelPercent	0	0	0	0	0	0	0
postExtinctionFlowChange-NitrogenPercent	0	0	0	0	0	0	0
postExtinctionFlowChange-RampTimeSec	0	0	0	0	0	0	0
postExtinctionFlowChangeHoldSec	0	0	0	0	0	0	0
Chamber & GC Operations							
chamber fill pressure (psia)	29.39	29.39	29.39	29.39	29.39	29.39	29.39
chamber fill O2%	40	40	40	40	40	40	40
chamber fill N2%	60	60	60	60	60	60	60
GC Sample Method (None, O2, Byproducts or Both)	-	-	-	-	-	-	-
Recirculation (i.e., scrub atmosphere) (After or No)	No	No	No	No	No	No	No
use HiBMS Camera?	No	No	No	No	No	No	No
HiBMS Binning	1x1	1x1	1x1	1x1	1x1	1x1	1x1
HiBMS Exposure (ms)	33	33	33	33	33	33	33
HiBMS Gain (V)	1	1	1	1	1	1	1
HiBMS Illumination Level (backlight)	0	0	0	0	0	0	0
dataCamera Zoom	25000	25000	45000	25000	25000	25000	25000
dataCamera Focus	14600	14600	10025	14600	14600	14600	14600
dataCamera Iris	0	0	0	0	0	0	0
dataCamera Filter	FS	FS	FS	FS	FS	FS	FS
Intensified Camera Frame Rate	23	23	23	23	23	23	23
Intensified Camera Filter	Form-aldehyde	Form-aldehyde	Form-aldehyde	Form-aldehyde	Form-aldehyde	Form-aldehyde	Form-aldehyde

Bibliography

- [1] P.G. Lignola, E. Reverchon, Cool flames, *Prog. Energy Combust. Sci.* 13 (1987) 75–96.
- [2] Y. Ju, C.B. Reuter, O.R. Yehia, T.I. Farouk, S.H. Won, Dynamics of cool flames, *Prog. Energy Combust. Sci.* 75 (2019) 100787.
- [3] J.F. Griffiths, S.K. Scott, Thermokinetic interactions: Fundamentals of spontaneous ignition and cool flames, *Prog. Energy Combust. Sci.* 13 (1987) 161–197.
- [4] H. Pearlman, R.M. Chapek, Cool flames and autoignition: thermal-ignition theory of combustion experimentally validated in microgravity, *Res. Technol.* 1999. (2000).
- [5] S.H. Won, B. Jiang, P. Diévert, C.H. Sohn, Y. Ju, Self-sustaining n-heptane cool diffusion flames activated by ozone, *Proc. Combust. Inst.* 35 (2015) 881–888.
- [6] G. Paczko, N. Peters, K. Seshadri, F.A. Williams, The role of cool-flame chemistry in quasi-steady combustion and extinction of n-heptane droplets, *Combust. Theory Model.* 18 (2014) 515–531.
- [7] V. Nayagam, D.L. Dietrich, P.V. Ferkul, M.C. Hicks, F.A. Williams, Can cool flames support quasi-steady alkane droplet burning?, *Combust. Flame.* 159 (2012) 3583–3588.
- [8] T.I. Farouk, F.L. Dryer, Isolated n-heptane droplet combustion in microgravity: “Cool Flames” – Two-stage combustion, *Combust. Flame.* 161 (2014) 565–581.
- [9] S. Thion, C. Togbé, Z. Serinyel, G. Dayma, P. Dagaut, A chemical kinetic study of the oxidation of dibutyl-ether in a jet-stirred reactor, *Combust. Flame.* 185 (2017) 4–15.
- [10] C.K. Law, P. Zhao, NTC-affected ignition in nonpremixed counterflow, *Combust. Flame.* 159 (2012) 1044–1054.
- [11] R.D. Reitz, Directions in internal combustion engine research, *Combust. Flame.* 160 (2013) 1–8.
- [12] S. Deng, D. Han, C.K. Law, Ignition and extinction of strained nonpremixed cool flames at elevated pressures, *Combust. Flame.* 176 (2017) 143–150.
- [13] T.I. Farouk, D. Dietrich, F.E. Alam, F.L. Dryer, Isolated n-decane droplet combustion – Dual stage and single stage transition to “Cool Flame” droplet burning, *Proc. Combust. Inst.* 36 (2017) 2523–2530.
- [14] N.L. Helgeson, M. Gerstein, B.P. Breen, Supersonic Aircraft Fuel Tank Fire Hazard Investigation, DYNAMIC SCIENCE MONROVIA CA, 1968.
- [15] T.C. Kosvic, L.B. Zung, M. Gerstein, Analysis of Aircraft Fuel Tank Fire and Explosion Hazards, DYNAMIC SCIENCE IRVINE CA, 1971.

- [16] R. Chapek, R. Tornabene, H. Pearlman, W. Sheredy, M.-S. Wu, The Cool Flames space-flight experiment, in: 2001 Conf. Exhib. Int. Space Stn. Util., n.d.: p. 5084.
- [17] J.H.E. Cartwright, Thermo-kinetic explosions: Safety first or safety last?, *Phys. Fluids*. 33 (2021) 031401.
- [18] V. Nayagam, D.L. Dietrich, M.C. Hicks, F.A. Williams, Cool-flame extinction during n-alkane droplet combustion in microgravity, *Combust. Flame*. 162 (2015) 2140–2147.
- [19] D.L. Dietrich, R. Calabria, P. Massoli, V. Nayagam, F.A. Williams, Experimental Observations of the Low-Temperature Burning of Decane/Hexanol Droplets in Microgravity, *Combust. Sci. Technol*. 189 (2017) 520–554.
- [20] T.I. Farouk, D. Dietrich, F.L. Dryer, Three stage cool flame droplet burning behavior of n-alkane droplets at elevated pressure conditions: Hot, warm and cool flame, *Proc. Combust. Inst.* 37 (2019) 3353–3361.
- [21] V. Nayagam, D.L. Dietrich, F.A. Williams, Effects of properties of atmosphere diluents on cool-flame combustion of normal-alkane droplets, *Combust. Flame*. 229 (2021) 111408.
- [22] X.L. Zheng, T.F. Lu, C.K. Law, C.K. Westbrook, H.J. Curran, Experimental and computational study of nonpremixed ignition of dimethyl ether in counterflow, *Proc. Combust. Inst.* 30 (2005) 1101–1109.
- [23] W. Sun, S.H. Won, Y. Ju, In situ plasma activated low temperature chemistry and the S-curve transition in DME/oxygen/helium mixture, *Combust. Flame*. 161 (2014) 2054–2063.
- [24] C.B. Reuter, M. Lee, S.H. Won, Y. Ju, Study of the low-temperature reactivity of large n-alkanes through cool diffusion flame extinction, *Combust. Flame*. 179 (2017) 23–32.
- [25] A. Alfazazi, A. Al-Omier, A. Secco, H. Selim, Y. Ju, S.M. Sarathy, Cool diffusion flames of butane isomers activated by ozone in the counterflow, *Combust. Flame*. 191 (2018) 175–186.
- [26] Y. Murakami, C.B. Reuter, O.R. Yehia, Y. Ju, Studies of autoignition-assisted nonpremixed cool flames, *Proc. Combust. Inst.* 38 (2021) 2333–2340.
- [27] O.R. Yehia, C.B. Reuter, Y. Ju, Low-temperature multistage warm diffusion flames, *Combust. Flame*. 195 (2018) 63–74.
- [28] O.R. Yehia, C.B. Reuter, Y. Ju, On the chemical characteristics and dynamics of n-alkane low-temperature multistage diffusion flames, *Proc. Combust. Inst.* 37 (2019) 1717–1724.
- [29] Y. Kang, Q. Wang, P. Zhang, C. Liu, X. Lu, Q. Wang, Study on flame structure and extinction mechanism of dimethyl ether spherical diffusion flames, *Energy*. 193 (2020) 116786.

- [30] P. Zhang, Y. Kang, X. Huang, S. Peng, Comparative Study on the Dimethyl Ether Combustion Characteristics in Normal and Inverse Diffusion Spherical Flame Geometries, *ACS Omega*. 5 (2020) 24654–24665.
- [31] A.G. Novoselov, C.B. Reuter, O.R. Yehia, S.H. Won, M.K. Fu, K. Kokmanian, M. Hultmark, Y. Ju, M.E. Mueller, Turbulent nonpremixed cool flames: Experimental measurements, Direct Numerical Simulation, and manifold-based combustion modeling, *Combust. Flame*. 209 (2019) 144–154.
- [32] D.P. Stocker, *ACME Engineering Implementation*, (2021).
- [33] P.H. Irace, H.J. Lee, K. Waddell, L. Tan, D.P. Stocker, P.B. Sunderland, R.L. Axelbaum, Observations of long duration microgravity spherical diffusion flames aboard the International Space Station, *Combust. Flame*. 229 (2021) 111373.
- [34] P. Dehghani, P.B. Sunderland, J.G. Quintiere, J.L. deRis, Burning in microgravity: Experimental results and analysis, *Combust. Flame*. 228 (2021) 315–330.
- [35] V. Nayagam, D.L. Dietrich, F.A. Williams, Partial-Burning Regime for Quasi-Steady Droplet Combustion Supported by Cool Flames, *AIAA J.* 54 (2016) 1235–1239.
- [36] P.H. Irace, H.J. Lee, K. Waddell, L. Tan, D.P. Stocker, P.B. Sunderland, R.L. Axelbaum, Observations of long duration microgravity spherical diffusion flames aboard the International Space Station, *Combust. Flame*. 229 (2021) 111373.
- [37] T.I. Farouk, D. Dietrich, F.E. Alam, F.L. Dryer, Isolated n-decane droplet combustion – Dual stage and single stage transition to “Cool Flame” droplet burning, *Proc. Combust. Inst.* 36 (2017) 2523–2530.
- [38] D.L. Dietrich, V. Nayagam, M.C. Hicks, P.V. Ferkul, F.L. Dryer, T. Farouk, B.D. Shaw, H.K. Suh, M.Y. Choi, Y.C. Liu, C.T. Avedisian, F.A. Williams, Droplet Combustion Experiments Aboard the International Space Station, *Microgravity Sci. Technol.* 26 (2014) 65–76.
- [39] K. Seshadri, N. Peters, F.A. Williams, V. Nayagam, G. Paczko, Asymptotic analysis of quasi-steady n-heptane droplet combustion supported by cool-flame chemistry, *Combust. Theory Model.* 20 (2016) 1118–1130.
- [40] A. Cuoci, A.E. Saufi, A. Frassoldati, D.L. Dietrich, F.A. Williams, T. Faravelli, Flame extinction and low-temperature combustion of isolated fuel droplets of n-alkanes, *Proc. Combust. Inst.* 36 (2017) 2531–2539.
- [41] M. Lee, Y. Fan, Y. Ju, Y. Suzuki, Ignition characteristics of premixed cool flames on a heated wall, *Combust. Flame*. 231 (2021) 111476.
- [42] G. Stockman, L.G. Shapiro, *Computer vision*, Prentice Hall PTR, 2001.
- [43] D.L. Dietrich, V. Nayagam, M.C. Hicks, P.V. Ferkul, F.L. Dryer, T. Farouk, B.D. Shaw, H.K. Suh, M.Y. Choi, Y.C. Liu, C.T. Avedisian, F.A. Williams, Droplet Combustion

Experiments Aboard the International Space Station, *Microgravity Sci. Technol.* 26 (2014) 65–76.

- [44] A. Cuoci, A.E. Saufi, A. Frassoldati, D.L. Dietrich, F.A. Williams, T. Faravelli, Flame extinction and low-temperature combustion of isolated fuel droplets of n-alkanes, *Proc. Combust. Inst.* 36 (2017) 2531–2539.
- [45] Z. Wang, P.B. Sunderland, R.L. Axelbaum, Dilution effects on laminar jet diffusion flame lengths, *Proc. Combust. Inst.* 37 (2019) 1547–1553.
- [46] J.C. Prince, F.A. Williams, Short chemical-kinetic mechanisms for low-temperature ignition of propane and ethane, *Combust. Flame.* 159 (2012) 2336–2344.
- [47] F.A. Williams, V. Nayagam, Quasi-steady combustion of normal-alkane droplets supported by Cool-Flame chemistry near diffusive extinction, *Combust. Theory Model.* 23 (2019) 748–770.